The Astrophysical Journal, 946:104 (24pp), 2023 April 1 https://doi.org/10.3847/1538-4357/acbcc1

Stellar Escape from Globular Clusters. I. Escape Mechanisms and Properties at Ejection

Newlin C. Weatherford[1,2], Fulya Kıroğlu[1,2], Giacomo Fragione[1,2], Sourav Chatterjee[3], Kyle Kremer[4,5], and Frederic A. Rasio[1,2]
[1] Department of Physics & Astronomy, Northwestern University, Evanston, IL 60208, USA
[2] Center for Interdisciplinary Exploration & Research in Astrophysics (CIERA), Northwestern University, Evanston, IL 60208, USA
[3] Tata Institute of Fundamental Research, Homi Bhabha Road, Mumbai 400005, India
[4] TAPIR, California Institute of Technology, Pasadena, CA 91125, USA
[5] The Observatories of the Carnegie Institution for Science, Pasadena, CA 91101, USA
Received 2022 November 29; revised 2023 February 2; accepted 2023 February 15; published 2023 April 5

Abstract

The theory of stellar escape from globular clusters (GCs) dates back nearly a century, especially the gradual evaporation of GCs via two-body relaxation coupled with external tides. More violent ejection can also occur via strong gravitational scattering, supernovae, gravitational wave-driven mergers, tidal disruption events, and physical collisions, but comprehensive study of the many escape mechanisms has been limited. Recent exquisite kinematic data from the Gaia space telescope has revealed numerous stellar streams in the Milky Way (MW) and traced the origin of many to specific MWGCs, highlighting the need for further examination of stellar escape from these clusters. In this study, the first of a series, we lay the groundwork for detailed follow-up comparisons between Cluster Monte Carlo GC models and the latest Gaia data on the outskirts of MWGCs, their tidal tails, and associated streams. We thoroughly review escape mechanisms from GCs and examine their relative contributions to the escape rate, ejection velocities, and escaper demographics. We show for the first time that three-body binary formation may dominate high-speed ejection from typical MWGCs, potentially explaining some of the hypervelocity stars in the MW. Due to their mass, black holes strongly catalyze this process, and their loss at the onset of observable core collapse, characterized by a steep central brightness profile, dramatically curtails three-body binary formation, despite the increased post-collapse density. We also demonstrate that even when born from a thermal eccentricity distribution, escaping binaries have significantly nonthermal eccentricities consistent with the roughly uniform distribution observed in the Galactic field.

Unified Astronomy Thesaurus concepts: Globular star clusters (656); Star clusters (1567); Stellar dynamics (1596); N-body simulations (1083); Tidal disruption (1696); Galactic archaeology (2178); High-velocity stars (736); Binary stars (154)

1. Introduction

As some of the largest, densest, and oldest stellar systems in the Milky Way (MW), globular clusters (GCs) have long attracted interest as windows not only into stellar dynamics, but also as tracers of Galactic evolution. Of the ∼170 known MWGCs (Vasiliev & Baumgardt 2021), most in the Galactic disk likely formed within giant molecular clouds early in the MW's history (e.g., Peebles & Dicke 1968), but a substantial fraction of those in the Galactic halo likely originated in satellites that have since merged with the MW. Suggestively, halo GCs feature higher velocity dispersion but lower circular velocity than disk GCs, as well as lower metallicity and more retrograde orbits (e.g., Searle & Zinn 1978; Rodgers & Paltoglou 1984; Zinn 1985, 1993; van den Bergh 1993; Da Costa & Armandroff 1995; Dinescu et al. 1999; Côté et al. 2000; Forbes & Bridges 2010). The MW's ongoing accretion of its satellites (Ibata et al. 1994; Martin et al. 2004; Belokurov et al. 2006) and their GCs (e.g., Bellazzini et al. 2003; Forbes et al. 2004) reinforces this scenario.

Recent astronomical surveys, especially the Gaia survey (Gaia Collaboration et al. 2021), have further revealed fine substructure in the MW halo, including numerous stellar streams (for a recent review and catalog, see Helmi 2020; Mateu 2023). These drawn-out associations of stars on similar orbits are likely debris from disrupted dwarf galaxies and their GCs, shorn off by Galactic tides during accretion by the MW. Gaia's exquisite kinematic data has firmly tied the origins of ∼10 especially thin streams to specific MWGCs (e.g., Myeong et al. 2018; Yuan et al. 2020; Bonaca et al. 2021; Ibata et al. 2021). Twin strands of stars termed tidal tails also emanate from some MWGCs, most famously extending far from Palomar 5 (e.g., Odenkirchen et al. 2001) into a full-fledged stream—but see Piatti & Carballo-Bello (2020) for a recent meta-analysis of many additional discoveries. These tails arise from the Coriolis effect in the rotating frame of a GC's orbit in the MW, which causes escapers headed toward (away from) the Galactic Center to speed ahead (trail behind) the GC (e.g., Binney & Tremaine 2008). Since tidal tails and stellar streams are excellent tracers of the MW's potential and recent merger history, their formation from stars escaping GCs is an essential topic in Galactic archeology.

While observational work on tidal tails and stellar streams is booming, theoretical study of stellar escape from GCs has a longer history. Numerous mechanisms (Section 2) cause high-speed escape, but low-speed escape via tides and two-body relaxation (e.g., Ambartsumian 1938; Spitzer & Shapley 1940; Chandrasekhar 1943) generally dominates in realistic GCs subject to external tides. Yet escape in this case is complex. In principle, escape occurs once a star crosses the GC's tidal

boundary, but this is neither guaranteed nor irreversible even for stars with high enough energies to do so. Back-scattering by encounters with other stars, the existence of periodic stellar orbits outside the tidal boundary, and the nonexistence of energy-based escape criteria for noncircular GC orbits add to the complexity (see the Appendix). These nuances challenge detailed study of escaper properties, especially comparison between theory and observation. Yet the Gaia survey and its impact on Galactic archeology provide ample opportunity and motivation for renewed effort. Such comparison is necessary to validate and improve the escape physics in GC modeling and explore in-cluster origins of field stars. It may also help constrain otherwise difficult-to-measure GC properties, such as the extent of central black hole (BH) populations, supernova (SN) kick strengths, and the stellar initial mass function, which all affect ejection speeds and the GC evaporation rate (e.g., Chatterjee et al. 2017; Weatherford et al. 2021).

In this study, the first in a series, we lay essential groundwork for direct comparison between Gaia observations and GC models simulated with the Cluster Monte Carlo code (CMC). We do so by exploring in-depth the various mechanisms of escape from GCs, especially their role in CMC. We analyze escapers from our recent catalog of CMC models (Kremer et al. 2020), focusing exclusively on properties at the time of removal from CMC, as opposed to the continued evolution of escaper trajectories in a full Galactic potential or any comparison to Gaia data—the focus of the second and third papers in this series, respectively.

We pay special attention to differences in escape before and after cluster *core collapse*. Our usage of this term refers to the *observable* transition from a flat (non-core-collapsed; NCC'd) to a steep (core-collapsed; CC'd) central surface brightness. This occurs upon dynamical ejection of the GC's central BH population, and corresponding transition from binary BH burning to binary white dwarf (WD) burning (e.g., Chatterjee et al. 2013; Kremer et al. 2019a, 2020, 2021; Rui et al. 2021a). *Binary burning* refers to hardening of binaries in encounters with passing stars (e.g., Heggie 1975; Hills 1975); the potential energy released by hardening heats the stars and the binaries' centers of mass, halting collapse. BH binaries, being the most massive, have more potential energy so are stronger heat sources. Yet especially dense GCs quickly eject BHs via strong encounters. Central heating then relies on (less massive) WDs, weakening binary burning and allowing the core to observably collapse (e.g., Kremer et al. 2019a, 2021). Note our usage is a refinement in detail to the conception of core collapse induced by the gravothermal instability (e.g., Spitzer 1987; Heggie & Hut 2003) and halted by three-body binary formation (3BBF). It also differs from the transient collapses characterizing *gravothermal oscillations* (e.g., Heggie & Hut 2003), in which the central regions of the cluster—especially BH populations (e.g., Morscher et al. 2013, 2015)—frequently and briefly contract via the gravothermal instability before re-expanding due to 3BBF. These mathematically chaotic oscillations occur throughout the GC's life, both before and after observable core collapse.

This paper is organized as follows. We first review numerous mechanisms of escape from GCs in Section 2 before describing our CMC models in Section 3. In Section 4, we examine escaper properties at the time of removal from CMC, emphasizing differences between CC'd and NCC'd GCs, as defined above. In particular, we analyze relative contributions from various escape mechanisms, distributions in ejection position and velocity, the escape rate over time, and properties of escaping binaries. We discuss the impact of 3BBF and limitations to our analysis in Section 5 and summarize our findings and the future direction of this series in Section 6. In the Appendix, we also include a short review of static tides and a comparative discussion of several escape criteria commonly used in modeling.

2. Escape Mechanisms

Here we broadly review the numerous mechanisms contributing to escape from star clusters. Though CMC features many of these mechanisms (Section 3.2), our intent is not merely to describe those we do study, but also to provide a fuller picture of the escape landscape. Prior studies on cluster escape rarely discuss more than a few mechanisms at once, and a comprehensive review has yet to appear in the literature; both factors motivate thorough discussion.

Escape from GCs can be split into two categories: ejection and evaporation (see Binney & Tremaine 2008, though our definitions are more expansive). *Ejection* occurs when a single dramatic event substantially increases the velocity of a cluster member all at once, potentially ejecting it with energy up to several times that necessary for escape. Events of this type include strong gravitational encounters—even collisions with other bodies—and assorted recoil kicks from stellar evolution, supernovae (SNe), tidal disruption events (TDEs), and gravitational-wave (GW)-driven mergers. In contrast, we define *evaporation* mechanisms to be those *incapable* of accelerating stars to speeds greatly in excess of the local escape speed. Mechanisms of this type include two-body relaxation and tidal stripping, which both operate on a macroscopic level—i.e., the key physics involves the cluster bulk rather than a single individual event or interaction. So they typically operate on timescales much greater than the dynamical timescale governing most (sudden) ejection mechanisms. Though evaporation mechanisms are less diverse than ejection mechanisms, they dominate the overall escape rate for realistic (tidally truncated) GCs, so we discuss them first.

2.1. Evaporation

The gradual evaporation of star clusters is a complex process given much attention over the years, including thorough discussions in classic field textbooks (e.g., Spitzer 1987; Heggie & Hut 2003; Binney & Tremaine 2008). We summarize key relevant features and note that our discussion differs slightly from earlier approaches; whereas many texts use *evaporation* to refer to escape via two-body relaxation (or *diffusion*), we expand this definition to include escape via global mass loss and time-dependent tides.

2.1.1. Two-body Relaxation

In a gravitational N-body system, the motions of each body introduce granular, time-dependent perturbations to the dominant, otherwise smooth underlying cluster potential. Via these fluctuations in the potential, the bodies exchange energy and momentum, causing each body to diffuse gradually and randomly through phase space. Though the exact trajectories obey the full set of coupled equations of motion, their numerical integration—as undertaken by direct N-body codes—is not especially instructive on a macroscopic level. The concept of two-body relaxation, specifically the

Chandrasekhar theory of relaxation (Chandrasekhar 1942, 1960; Spitzer 1987; Heggie & Hut 2003; Aarseth et al. 2008; Binney & Tremaine 2008) applies the simplifying approximation that the net diffusive effect of these perturbations is capturable as the sum of many *weak*, *impulsive*, and *uncorrelated* two-body encounters. The meaning of *weak* in this context is that each such encounter is distant enough to change the bodies' velocities v by only a small amount ($\Delta v/v \ll 1$). Many such weak encounters cumulatively change v by of order itself ($\Delta v/v \sim 1$) on the relaxation timescale—e.g., Equation (2.62) in Spitzer (1987):

$$t_r \approx \frac{0.065\langle v\rangle^3}{G^2\langle n\rangle\langle m\rangle^2 \ln\Lambda}. \quad (1)$$

Here $\langle v\rangle$, $\langle n\rangle$, and $\langle m\rangle$ are the average velocity, number density, and stellar mass, respectively, while the Coulomb logarithm $\ln\Lambda \approx \ln(N/100)$ accounts for the range of impact parameters and depends on the initial mass function (e.g., Freitag et al. 2006; Rodriguez et al. 2018c). Due to the spread in v, n, and m, the local t_r is often several orders of magnitude longer in the GC's sparse halo than at its center, but the above is a reasonable fiducial timescale for the entire cluster.

As a random-walk process, relaxation drives the velocity distribution function (DF) toward thermal equilibrium, i.e., a Maxwellian DF. Bodies inevitably wander into the DF's high-speed tail, where a final weak encounter may push them beyond the cluster's local escape speed. Though later encounters will drive some back down to lower energy, rebinding them to the GC before long (e.g., King 1959), many will eventually escape altogether. Crucially, the escape of these bodies evacuates the DF's high-speed tail, shifting the GC back away from equilibrium and encouraging more bodies to refill the tail. These, too, escape and the process repeats. The decline in cluster mass, aided by stellar evolution mass loss (e.g., Chernoff & Weinberg 1990), further enhances this cycle by continuously raising the GC's potential and decreasing the escape speed. So gravitational N-body systems never reach equilibrium[6] and have finite lifetimes dependent on t_r (e.g., Ambartsumian 1938; Spitzer & Shapley 1940). Back-scattering of *potential escapers* back down to lower energy grows more efficient with lower N, increasing cluster lifetime (Baumgardt 2001).

2.1.2. Cluster Mass Loss

As noted above, the very act of losing mass raises (makes less negative) the cluster potential, thereby reducing the escape speed. So by unbinding stars already near the escape speed, mass loss can in principle be considered its own evaporation mechanism—especially when due to stellar evolution (e.g., Chernoff & Weinberg 1990), since it relies on no *other* escape mechanisms to reduce the cluster mass (see also Section 7.5.1 of Binney & Tremaine 2008). However, since cluster mass loss and two-body relaxation are both continuous, global phenomena, not discrete events like ejection during close encounters, it is impossible to definitively distinguish between these mechanisms when attributing the cause of escape for any specific body. Note the same degeneracy applies to time-dependent tides below, but unlike cluster mass loss and relaxation, these are often left out of cluster models.

2.1.3. Sharply Time-dependent Tides

Star clusters also evaporate via global tidal effects—large-scale external perturbations to the cluster's gravitational potential. The simplest scenario, often used in modeling, is a cluster in a circular galactocentric orbit in an unchanging, spherical galactic potential. In this case, the galactic potential is static in the frame corotating with the orbit and imposes on the cluster a nonspherical tidal boundary (*not* static since the cluster still loses mass). This eases escape via other mechanisms by lowering the escape energy (see Appendix A.1). However, without simultaneous internal energy exchange or mass loss via gravitational scattering or stellar evolution, there is no way for a static external tide to independently unbind cluster members. So to count as a truly distinct evaporation mechanism tides must be *time dependent*.

Realistic tidal fields are time dependent in several ways. For example, the orbits of most MWGCs are both somewhat eccentric and inclined relative to the Galactic disk (e.g., Baumgardt et al. 2019). The former causes the Galactic tide to strengthen at perigalacticon, while the latter causes it to strengthen during passage through the Galactic disk (e.g., Ostriker et al. 1972; Spitzer & Chevalier 1973). Similar perturbations occur during passage near any other mass within the Galaxy, including other GCs or giant molecular clouds (e.g., Gieles et al. 2006). Except in cases of nearly adiabatic time dependence, such as slow evolution of the galactic potential itself, any of these external perturbations to the cluster potential can induce *tidal shocks* that heat the cluster through differential acceleration of individual stars relative to the cluster center (see discussions in Spitzer 1987; Heggie & Hut 2003; Binney & Tremaine 2008).

Like two-body relaxation, tidal shocking can cause escape. Indeed, direct N-body models show that mass loss is significantly faster in GCs with highly eccentric and/or inclined orbits, in part due to shocking (e.g., Baumgardt & Makino 2003; Webb et al. 2013, 2014; Madrid et al. 2014). To significantly affect a star's orbit within the cluster, the shocks must be relatively impulsive (occur on a timescale less than the star's orbital period). This is especially likely in the cluster halo, where the crossing time is longer. Shock heating may even exceed heating from two-body relaxation in the halos of disk-crossing GCs (e.g., Kundic & Ostriker 1995; Gnedin & Ostriker 1997; Gnedin et al. 1999a, 1999b), but the latter dominates in all but the most massive GCs (e.g., Fall & Zhang 2001; McLaughlin & Fall 2008; Prieto & Gnedin 2008).

2.2. Ejection

There are many ways to eject objects from star clusters in individual, dramatic, potentially violent events. So it serves us well to further divide ejection mechanisms into three classes: strong encounters, (near-)contact recoil, and stellar evolution recoil. Fundamentally, the second is simply a more extreme extension of the first that may involve elements of the third. In general, keep in mind these mechanisms are not mutually exclusive, though stellar evolution recoil is conceptually distinct by not relying on gravitational scattering.

[6] More generally, the gravothermal catastrophe (e.g., Lynden-Bell et al. 1968; Heggie & Hut 2003; Binney & Tremaine 2008) prevents *any* finite gravitational system from reaching thermal equilibrium; cooling bodies simply sink deeper into the potential, causing them to speed up faster than they cool. This also prevents equipartition of (kinetic) energy, since heavier bodies sink via dynamical friction, causing them to heat rather than cool.

2.2.1. Strong Encounters

Strong gravitational scattering interactions are some of the most well-studied ejection mechanisms, featuring close passages between two or more bodies or bound hierarchies (e.g., binaries and triples) that may apply large dynamical kicks to one or more bodies. Kick magnitudes have large variance, depending strongly on the relative speed and orientations of the interacting bodies/hierarchies. Strong encounter ejection mechanisms include the following:

1. *Strong two-body encounters*. Weak perturbations dominate the *average* rate of energy change experienced by cluster members in two-body scattering, enabling the classic relaxation theory described above. The result is a relatively smooth random walk in each body's orbital energy, unable to induce velocities much larger than the cluster's local escape speed. However, the true random walks are sharper and more granular—more conducive to high-speed ejection. In the right circumstances (e.g., a flyby of a much more massive object on a similar trajectory), a single close encounter can be much stronger —up to $\Delta v/v \approx 3$ (e.g., Hénon 1969). Though rare, such encounters would have outsize influence on the high-velocity end of the ejection speed distribution, and are not captured by standard two-body relaxation. The impact of strong two-body encounters is greater in isolated clusters, where relaxation is less effective at causing escape (Hénon 1960, 1969; Spitzer & Shapiro 1972).
2. *Three-body encounters between singles*. Strong encounters between *three* separate bodies are rarer than between two. Yet they dominate new binary formation (e.g., Heggie & Hut 2003) since two of the bodies often bind together, with increasing probability for stronger encounters (Aarseth & Heggie 1976). The potential energy released in binding accelerates the leftover single and the new binary's center of mass. These kicks can easily eject the single from the cluster. (Binary ejection is rare since those formed this way are biased to much higher mass than the leftover single and so receive smaller kicks under momentum conservation; see Section 5.1.) Even the encounters that do *not* form binaries can still cause ejection, albeit at lower speeds due to the lesser release of potential energy. Yet strong encounters between three singles have attracted little attention due to their rarity for typical stellar masses in even dense GCs. This reasoning neglects the encounter rate's exceptional sensitivity to the masses and velocities of the species involved. Central BH populations in GCs especially enhance three-body binary formation (e.g., Kulkarni et al. 1993; O'Leary et al. 2006; Morscher et al. 2013, 2015). In Section 4.1, we show this enhancement may allow 3BBF to dominate high-speed stellar escape from MWGCs at present.
3. *Binary–single encounters*. Three-body encounters between a binary and a single also commonly lead to large dynamical kicks. In particular, the flyby of a single star near a sufficiently hard (compact) binary tends to further harden the binary, the released potential energy again boosting the speeds of the single and binary center of mass (e.g., Heggie 1975; Hills 1975; Sigurdsson & Phinney 1993). When a three-body interaction involving a hard binary features a high mass ratio, ejection speeds of several hundred kilometers per second are possible (e.g., Gvaramadze et al. 2009) and help explain the high observed velocities of O- and B-type stars in the MW (e.g., Fujii & Zwart 2011).
4. *Binary–binary encounters*. Strong four-body encounters involving two binaries are rarer than binary–single encounters due to the limited binary fraction in a GC's dense core (e.g., Milone et al. 2012). However, by providing additional binding energy to transfer into orbital speeds and another star to prolong resonance interactions featuring especially close pericenter passages, binary–binary scattering can cause very high-speed ejections of order several hundred kilometers per second (e.g., Leonard & Duncan 1988, 1990; Gualandris et al. 2004), potentially above 10^3 km s^{-1} (e.g., Leonard 1991).
5. *Higher-N* encounters. The above reasoning extends to paired interactions between larger-N bound hierarchies (triple–single, triple–binary, etc.), higher-multiplicity single interactions (e.g., four-body binary formation), or some combination (e.g., binary–single–single)—in principle up to the size of the GC. But as hierarchy size and interaction multiplicity grow, the encounter rate rapidly diminishes in typical GCs, too dense to accommodate durable hierarchies yet too diffuse to feature appreciable rates of high-multiplicity strong encounters (e.g., Atallah et al. 2022). From a practical standpoint, direct N-body codes implicitly incorporate these physics by fully integrating trajectories, while introducing higher-N encounters into alternatives like Monte Carlo or Fokker–Planck codes would quickly erode their main advantage—computational speed. So while higher-N encounters may allow slightly more or higher-speed ejections—due to the remote chance of chained gravitational slingshots like those used in spacecraft maneuvers —any increase is likely small.
6. *Unstable triple disintegration*. Triples and larger hierarchies are ephemeral in typical GCs but present a unique ejection mechanism beyond encounters with other bodies. Triples can be unstable to gravitational perturbations or stellar mass loss (e.g., Mardling & Aarseth 2001). When instability causes them to disintegrate (typically into a binary and single), the released binding energy can accelerate the separating bodies by tens to hundreds of kilometers per second (Toonen et al. 2022).

2.2.2. (Near-)Contact Recoil

Ejection physics is more complex when objects pass *so* close that tides, internal stellar processes, and/or relativistic effects are relevant. Such strong encounters often feature direct contact between two bodies or nearly so. As with the strong encounters above, the encounter rate increases with number density and stellar mass, but the latter's influence is amplified since the intrinsic size of each body, which typically increases with mass, now matters. Binaries also greatly enhance the rates due to their large cross sections and since strong encounters involving them are often *resonant*, featuring chaotic series of many separate pericenter passages (e.g., Bacon et al. 1996; Fregeau et al. 2004).

1. *Direct physical collisions*. From the standpoint of distance, the strongest gravitational interaction two bodies may experience is a rare head-on collision. Though much of the released gravitational energy goes

into the internal energy of the collision remnant(s), asymmetric mass ejection during the collision can kick the remnant(s), and by momentum conservation, any other bodies in the interaction. Hydrodynamic simulations suggest such kicks can reach $\sim$10 km s^{-1} in star–star collisions (Gaburov et al. 2010) or even up to $\sim$100 km s^{-1} in BH–star collisions (Kremer et al. 2022a). In general, however, the kick speeds depend sensitively on the exact species and processes involved.

2. *TDEs*. Less extreme than a physical collision is a TDE, in which a star passes close enough to another body for that body to strip away some of the star's mass, potentially even destroying it entirely (e.g., Rees 1988; Kremer et al. 2019b; Samsing et al. 2019; Fragione et al. 2021). If the mass loss is asymmetric, the TDE also kicks the remnant (s). Hydrodynamic simulations suggest mass loss during the tidal capture of a star into a binary with a BH (or complete disruption of the star) can kick the new binary's center of mass (or, for full disruptions, the leftover lone BH) by $\sim$10–100 km s^{-1} (Kremer et al. 2022a). The kick is typically highest for more-penetrating encounters, which cause more mass loss. Similar kicks can apply directly to the unbound stellar remnant itself and more extreme kicks at several hundred kilometers per second can occur in TDEs during encounters between tight stellar binaries and BHs (Ryu et al. 2023) or even at $\gtrsim 10^3$ km s^{-1} in TDEs involving 10^2–$10^4\,M_\odot$ intermediate-mass BHs (IMBHs; Kıroğlu et al. 2022). Kicks from asymmetric mass loss have also been studied in the context of planets (Faber et al. 2005; Guillochon et al. 2011; Liu et al. 2013), main-sequence (MS) stars (Manukian et al. 2013; Gafton et al. 2015; Ryu et al. 2020a, 2020b, 2020c), WDs (Cheng & Evans 2013), and neutron stars (NSs; Rosswog et al. 2000; Kyutoku et al. 2013; Kremer et al. 2022b).
3. *GW-driven mergers*. Finally, mergers driven by GW dissipation, in particular BH mergers, emit GWs asymmetrically, often kicking the remnant by tens to hundreds of kilometers per second (e.g., Bonnor & Rotenberg 1961; Peres 1962; Bekenstein 1973; Favata et al. 2004; Merritt et al. 2004a; Lousto & Zlochower 2008, 2009, 2011; Lousto et al. 2010, 2012). This notably hinders IMBH growth via BH mergers in star clusters, as the kick often ejects the remnant except at extreme mass ratios—such as a low-mass BH merging with a preexisting IMBH (e.g., Holley-Bockelmann et al. 2008; Moody & Sigurdsson 2009; Morawski et al. 2018; Rasskazov et al. 2020; Arca Sedda et al. 2021; Fragione & Loeb 2021; Fragione et al. 2022a, 2022b; González Prieto et al. 2022; Maliszewski et al. 2022).

2.2.3. Interactions with IMBHs

IMBHs in the range of 10^2–$10^4\,M_\odot$, if present in a GC, may strongly affect cluster evolution and ejection speeds (e.g., Baumgardt et al. 2005; Baumgardt 2017). Interactions with IMBHs do not necessarily constitute a separate ejection mechanism, since they are just a more extreme case of strong encounters or TDEs involving typical stellar BHs. Yet this channel is worth highlighting for its potential to help identify IMBHs in GCs.

The process of disrupting a stellar binary via a binary–single strong encounter with a massive BH (classically a supermassive BH) is often known as the Hills mechanism (Hills 1988), though note this is merely an extreme case of an ordinary stellar binary–single encounter. The tidal radius of the BH is $r_t \sim (M/m)^{1/3} a$, where M is the BH mass, $m = m_1 + m_2$ the binary mass, and a the binary semimajor axis. When the binary comes within distance r_t of the BH, it is typically disrupted, leaving one star bound to the BH and ejecting the other at high speed. Recently, Fragione & Gualandris (2019) demonstrated that for typical stellar masses and binary semimajor axes in the core of a GC, a $10^3\,M_\odot$ IMBH at the GC's center would eject stars at speeds most commonly near 700 km s^{-1} and up to $>10^3$ km s^{-1}. An earlier rate analysis by Pfahl (2005) and reexamined by Fragione & Gualandris (2019) suggests that a typical GC hosting a $10^3\,M_\odot$ IMBH would eject such stars at a rate of $\approx$0.1 Myr^{-1}, yielding a highly significant contribution to the high-speed ejection distribution of a GC. As discussed above, TDEs by IMBHs can also lead to high-speed stellar ejections (Kıroğlu et al. 2022). Possible instances of each of these mechanisms have already been observed (e.g., Gualandris & Portegies Zwart 2007; Lin et al. 2018). So, while we do not examine this channel in this study, high-speed ejecta from MWGCs may eventually provide a valuable constraint on retention of IMBHs in specific MWGCs.

2.2.4. Stellar Evolution Recoil

Stellar evolution preceding/during the birth of compact objects can also cause ejection. In particular, SNe that form NSs and BHs may feature asymmetric ejection of matter, giving their remnants impulsive recoil kicks known as SNe kicks. By momentum conservation, these kicks may also eject binary companions to SNe progenitors—in fact, Blaauw (1961) originally proposed SNe kicks to explain speedy O- and B-type stars, suggesting they were once binary companions to SNe progenitors. Asymmetric stellar winds may even propel WD progenitors. We detail several subtypes of stellar evolution recoil below.

SNe kicks in isolation. The simplest case of SN-induced ejection from clusters occurs when the progenitor star exists in isolation (i.e., not a member of a binary or higher-order bound hierarchy). In such cases, the SN kick simply changes the velocity of the compact remnant itself, often by enough to eject it from the cluster, leaving it as a lone dark object.

1. *NS SNe kicks* are the strongest and most observationally supported form of stellar evolution recoil. Empirical evidence for these kicks exists in the high velocity dispersion of the pulsars (e.g., Lyne et al. 1982; Lyne & Lorimer 1994; Hansen & Phinney 1997; Arzoumanian et al. 2002; Hobbs et al. 2005) or otherwise-observable NSs of the MW (e.g., those detectable via nebular bow shocks; Cordes et al. 1993). Typical kick magnitudes are hundreds of kilometers per second, which can be strong enough to eject NSs from galaxies, let alone star clusters. Consequently, most NSs escape their host clusters at birth.
2. *BH SN kick* magnitudes are more uncertain but are plausibly lower than NS kicks due to additional fallback of ejected mass onto the SN remnant. Indeed, the positions and velocities of BH X-ray binaries (XRBs)

in the MW suggest that while at least some BHs receive SNe kicks of $\sim$100 km s^{-1}, many likely receive lesser or negligible kicks (e.g., Repetto et al. 2017, and references therein). While such speeds are sufficient to eject many BHs, the observed range of XRB velocities is consistent with significant BH retention in GCs (e.g., Chatterjee et al. 2017). Further observational support for such retention has been found in GCs' surface brightness and velocity dispersion profiles and internal mass segregation (e.g., Merritt et al. 2004b; Mackey et al. 2007, 2008; Peuten et al. 2016; Arca Sedda et al. 2018; Askar et al. 2018; Kremer et al. 2018, 2019a, 2020; Weatherford et al. 2018, 2020; Zocchi et al. 2019; Rui et al. 2021a). BH microlensing events may soon provide more detailed constraints on natal kick speeds (e.g., Andrews & Kalogera 2022).

SNe kicks in binaries. Various escape outcomes are possible when an SN takes place in a binary (see, e.g., Appendix A1 of Hurley et al. 2002, for a quantitative description). Depending on its strength and direction, the raw kick experienced by the SN remnant may be weak enough to drag its binary companion with it, resulting in a weaker effective kick to the center of mass of the binary, still bound together but with altered orbital parameters. The raw SN kick may even be strong enough to fully unbind the binary, reducing the SN remnant's final speed but applying an *induced kick* to the companion. This leads to the following ejection scenarios:

1. *Binary ejection*. In this case, the raw SN kick is not enough to unbind the binary but is large enough to eject it from the cluster, for example, as an XRB or even doubly compact binary.
2. *Binary disruption*. Alternatively, kicks great enough to unbind the binary may also eject either the SN remnant or its companion, often both. A key difference between this scenario and the isolated SN ejection scenario above is that while the SN remnant again escapes on its own, it does so at reduced speed, as unbinding the binary consumes some of the kick's energy.
3. *SN-induced (near-)contact recoil*. Finally, when the SN kicks the remnant toward its companion, it may physically collide with or tidally disrupt the companion, yielding similar scenarios to the dynamically induced mechanisms discussed in Section 2.2.2.

WD kicks. WDs may also experience stellar evolution recoil under certain circumstances. In particular, asymmetric mass loss during the asymptotic giant branch (AGB) phase of stellar evolution may gently propel a WD progenitor. (Note this may also affect a BH or NS progenitor during its AGB phase, but less impactfully since the SN kick shortly thereafter would likely dwarf such propulsion.) If true, this would help explain a variety of WD observations, including an underabundance in open clusters (e.g., Weidemann 1977; Kalirai et al. 2001; Fellhauer et al. 2003), wide spatial distribution, and low velocity dispersion in GCs (e.g., Heyl 2007, 2008a, 2008b; Calamida et al. 2008; Davis et al. 2008), and unexpectedly wide semimajor axes among WD-containing binaries observed with Gaia (El-Badry & Rix 2018). Each finding tenuously supports nonzero WD birth kicks, though no more than a few kilometers per second. This would only be large enough to eject WDs already relatively near their host GC's local escape speed. Alternatively, some actively accreting WDs may experience *failed* Type 1a SNe capable of larger kicks of $\sim$100 km s^{-1} (e.g., Jordan et al. 2012), though this kick magnitude is highly uncertain (e.g., Kromer et al. 2013).

3. Cluster Models

We simulate MWGCs using `CMC` (for `Cluster Monte Carlo`), a Hénon-type (Hénon 1971a, 1971b) Monte Carlo code for star cluster modeling (see Rodriguez et al. 2022, for the most recent and thorough overview). `CMC` includes prescriptions for numerous physics essential to the evolution of massive GCs, including stellar evolution (comments below), two-body relaxation (Joshi et al. 2000; Pattabiraman et al. 2013), galactic tidal fields (Joshi et al. 2001; Chatterjee et al. 2010), three-body binary formation (Morscher et al. 2013, 2015), physical collisions (Fregeau & Rasio 2007), and strong three- and four-body scattering (Fregeau et al. 2003; Fregeau & Rasio 2007) performed with the small-N direct integrator `fewbody`, which includes post-Newtonian dynamics (Fregeau et al. 2004; Antognini et al. 2014; Amaro-Seoane & Chen 2016; Rodriguez et al. 2018a, 2018b). `CMC` also allows for two-body binary formation through GW and tidal capture (Kremer et al. 2020; Ye et al. 2022), but only the former is included in the models used here.

We limit our analysis to a subset of 12 GC simulations (see Table 1) from our larger `CMC` Cluster Catalog (Kremer et al. 2020). Each begin with an initial number of particles (single stars plus binaries) $N_i = 8 \times 10^5$ and cluster metallicity $Z/Z_\odot = 0.1$. The chosen N_i yields GCs near the average of the present-day MWGC mass distribution (e.g., Mandushev et al. 1991; Hilker et al. 2020) and Z is similarly typical of MWGCs (e.g., Harris 1996, 2010 edition). In these simulations, we only vary the initial virial radius $r_v/\mathrm{pc} \in [0.5, 1, 2, 4]$ and Galactocentric distance $R_g/\mathrm{kpc} \in [2, 8, 20]$, also designed to capture the spread of MWGCs (Kremer et al. 2020). Yet due to the highly detailed nature of this study focusing on escape mechanisms and demographics, we devote most of our attention to two archetypal GC models: the two most representative of typical CC'd and NCC'd MWGCs (models 2 and 8 in Table 1, respectively). These differ in only their initial virial radius ($r_v/\mathrm{pc} = 0.5, 2$), which controls the initial density and hence the timescales for relaxation and dynamical ejection of central BHs. Recall the latter induces core collapse as defined in Section 1—the transition from a flat to a steep central surface brightness and long-term contraction of the core radius r_c. In the following sections, we use the *theoretical* density-weighted r_c from Casertano & Hut (1985). Not only does this shrink when the central surface brightness steepens, it is also more sensitive to transient density oscillations among central compact objects than measures based solely on surface brightness or cumulative luminosity profiles (Chatterjee et al. 2017).

In each simulation, the randomized initial positions and velocities derive from a King (1966) profile with concentration $w_0 = 5$. Stellar masses (primary mass m_p, in the case of a binary) draw from the standard Kroupa (2001) initial mass function from 0.08–150 $M_\odot$. Binary sampling proceeds by randomly assigning secondaries to $N \times f_b$ stars, independent of radial position or mass, where $f_b = 5\%$. Secondary masses adopt a uniform mass ratio $q \in [0.08/m_p, 1]$ and binary orbital periods draw from a distribution flat in log-scale (e.g., Duquennoy & Mayor 1991), where the orbital separations range from near contact to the hard/soft boundary. Binary

Table 1
Initial/Final Cluster Properties and Final Population Counts

	Simulation from the CMC Cluster Catalog	r_v (pc)	R_g (kpc)	r_c (pc)	r_h (pc)	r_t (pc)	$v_{esc,0}$ (km s^{-1})	Final Population Counts					
								MS	G	WD	NS	BH	Total
1	N8-RV0.5-RG2-Z0.1	0.5	2	0.11	3.89	28.9	32.0	316,698	1612	62,257	248	1	365,516
2	N8-RV0.5-RG8-Z0.1	0.5	8	0.14	4.87	82.7	35.0	535,190	2073	78,615	278	0	591,369
3	N8-RV0.5-RG20-Z0.1	0.5	20	0.18	5.28	156.6	35.4	598,223	2214	83,547	307	1	656,581
4	N8-RV1-RG2-Z0.1	1	2	1.03	3.97	31.3	24.9	437,164	2028	73,153	202	20	489,449
5	N8-RV1-RG8-Z0.1	1	8	1.22	4.85	85.7	26.2	617,548	2306	84,467	237	25	673,931
6	N8-RV1-RG20-Z0.1	1	20	1.44	5.26	160.5	25.6	659,786	2365	86,974	243	33	717,040
7	N8-RV2-RG2-Z0.1	2	2	2.62	5.86	30.4	16.8	400,030	1850	66,439	112	72	447,165
8	N8-RV2-RG8-Z0.1	2	8	2.79	7.00	86.9	20.3	654,814	2346	85,668	160	89	710,590
9	N8-RV2-RG20-Z0.1	2	20	2.93	7.58	161.7	20.6	730,566	3246	74,113	166	119	773,267
10	N8-RV4-RG2-Z0.1	4	2					*Disrupted*					
11	N8-RV4-RG8-Z0.1	4	8	4.78	11.1	87.4	16.8	661,605	2358	84,716	75	269	715,520
12	N8-RV4-RG20-Z0.1	4	20	4.99	11.6	163.2	16.7	693,645	2437	87,763	106	285	749,357

Note. Initial virial radius r_v, Galactocentric distance R_g, and final core, half-mass, and tidal radii (r_c, r_h, and r_t, respectively), central escape speed $v_{esc,0}$, and in-cluster population counts for MS = main-sequence stars, G = giants, WD = white dwarf, NS = neutron star, BH = black hole, and their combined total. Simulation 10 is excluded from the final counts since it disrupted long before a Hubble time.

eccentricities are thermal (Heggie 1975) and we allow each GC simulation to evolve to a final time of 14 Gyr.

Simulations from the CMC Cluster Catalog implement stellar evolution via the single/binary-star evolution codes SSE/BSE (Hurley et al. 2000, 2002), with recent prescriptions for wind-driven mass loss, compact object formation, and pulsational-pair instability (see Kremer et al. 2020). While minor enhancements have since been and continue to be implemented into the latest publicly available version of CMC—now via the stellar evolution code COSMIC (Breivik et al. 2020), an SSE/BSE derivative—such enhancements are largely irrelevant for this study focusing on escape mechanisms. When ongoing stellar evolution after escape becomes relevant for constructing extra-tidal observables in our follow-up work (Weatherford et al. 2023, in preparation), we continue evolving escapers with COSMIC.

3.1. Tidal Truncation and Escape in CMC

By default, CMC models are tidally limited under the assumption that the clusters circularly orbit the Galactic Center with circular speed $V_G = \Omega R_G = 220\,\mathrm{km\,s^{-1}}$, typical of MWGCs (e.g., Binney & Tremaine 2008). CMC defines its tidal radius as $r_t \equiv r_J$, utilizing the more accurate calculation of the Jacobi radius r_J for a realistic logarithmic Galactic potential (see Appendix A.1), leading to (e.g., Spitzer 1987; Baumgardt & Makino 2003; Chatterjee et al. 2010)

$$r_t(t) \equiv \left(\frac{M_C(t)}{2M_G}\right)^{1/3} R_G = \left(\frac{GM_C(t)}{2V_G^2}\right)^{1/3} R_G^{2/3}. \quad (2)$$

Note the explicit time dependence through the cluster mass, which decreases via both stellar escape and stellar winds.

To determine escape, CMC uses an energy-based criterion (Giersz et al. 2008) tuned to reproduce well the escape rate from direct N-body models. This criterion modifies the standard energy criterion (Appendix A.1) to account for back-scattering of *potential* escapers down to lower energies before they can cross the tidal boundary. Specifically, CMC immediately removes any particles with specific energy greater than the cluster potential at r_t times an order unity factor,

$$E > \alpha\phi_c(r_t), \quad (3)$$

where the factor α, tuned by comparison to direct N-body models, is given by

$$\alpha \equiv 1.5 - 3\left(\frac{\ln\Lambda}{N}\right)^{1/4}. \quad (4)$$

Here, $\ln\Lambda = \ln(\gamma N)$ is the Coulomb logarithm. In CMC, γ defaults to 0.01 (see also Freitag et al. 2006; Rodriguez et al. 2018c, 2022). Numerical testing (Giersz et al. 2008; Chatterjee et al. 2010) has shown that Equation (3) produces significantly better agreement to direct N-body simulations than alternatives, such as simply stripping stars with apocenters beyond the tidal boundary (for further discussion, see Appendix A.2).

3.2. Escape Mechanisms in CMC

CMC features many of the escape mechanisms in Section 2, as neatly listed in Table A1. The implementation of two-body relaxation and several types of strong interactions—binary–single and binary–binary encounters, 3BBF, and physical collisions—features extensively in Rodriguez et al. (2022) and references therein. Regarding 3BBF especially, we note that while earlier CMC models (since Morscher et al. 2013) only allowed 3BBF between three BHs, the CMC Cluster Catalog models allow this process between any three bodies, as is generally possible (though one or more BHs are usually involved; see Section 4.2). Meanwhile, physical collisions in CMC use a simplified sticky-sphere approximation, occurring whenever the radii of any two bodies (except NSs or BHs) overlap, at which point the bodies merge with partial mass loss if one is a WD and no mass loss otherwise. A collision between a BH/NS and any other star entirely destroys the latter without affecting the NS/BH mass. In all cases, the collisions conserve total momentum and assume any mass loss is spherically symmetric, so no kicks from asymmetric matter ejection apply to the collision remnant. This guarantees the remnant has speed $v < v_{esc}$ unless one of the colliding bodies already had $v > v_{esc}$, so we do not count collisions as a true escape mechanism in

CMC. Related CMC prescriptions for TDEs are in development and not included either. Similarly, while CMC allows for time-dependent tidal fields (input at simulation start as a table describing a time-varying tidal tensor, e.g., Rodriguez et al. 2023), we leave examination of these effects for later studies.

As for other scattering-driven escape mechanisms, CMC does not yet account for strong two-body encounters or higher-N hierarchies/interaction multiplicities (e.g., triples or four-body binary formation). While triples do form in fewbody, CMC simply breaks them apart at the end of each time step, so they do not participate in global dynamics (for further discussion, see Fragione et al. 2020). Since CMC passes the released binding energy to neighboring stars this technically *can* cause escape—implicitly lumped in with relaxation in this study. It is merely doubtful that such an artificial approach faithfully mimics ejection via triple disruption, especially the ejection speed distribution.

CMC does include prescriptions for GW-driven mergers and SNe kicks, however. Specifically, CMC treats binary BH mergers—including product mass, spin, and recoil kick—with formulae, fitted to numerical relativity simulations, from Gerosa & Kesden (2016). For further details, see Rodriguez et al. (2018a, 2018b). SNe prescriptions draw from the *rapid* model by Fryer et al. (2012) for standard iron core-collapse SNe (CCSNe) and from Belczynski et al. (2016) for pair-instability and pulsational-pair-instability SNe. Electron-capture SNe (ECSNe) from several channels—including accretion- or merger-induced collapse of WDs—also feature in CMC (Ye et al. 2019). The NS recoil kicks $V_{\rm NS}$ draw from Maxwellians with dispersions $\sigma = 265\,{\rm km\,s^{-1}}$ (CCSNe) or $\sigma = 20\,{\rm km\,s^{-1}}$ (ECSNe). The BH kicks follow the NS kick distribution for CCSNe, but reduced according to the fraction $f_{\rm fb}$ of the progenitor's stellar envelope that falls back onto the BH remnant: $V_{\rm BH} = V_{\rm NS}(1 - f_{\rm fb})$. For further details, see Kremer et al. (2020) and note in contrast that since evidence for significant WD kicks remains tenuous, CMC does not include them. Finally, since stellar evolution in CMC occurs concurrently with fewbody, SNe kicks conserve momentum in the integrator, allowing for more complex ejection mechanisms like SN-induced binary ejection or disruption and SN-induced (near-)contact recoil.

3.2.1. Classifying Escape Mechanisms in Post-processing

In Section 4, we classify escapers by escape mechanism based on detailed CMC output—notably logs of all fewbody interactions, 3BBF, collisions, BH-forming SNe, BH mergers, and SN-induced binary disruption events. To determine the escape mechanism for each escaper (single or binary), we search each of the aforementioned log files for an event involving that body (component bodies in the case of a binary) at the time of removal from CMC. If the body or binary components do not appear in any of the log files at the appropriate time, process of elimination attributes the cause of escape to relaxation—implicitly coupled with static tides and triple disintegration, as explained earlier. Since simulations from the CMC Cluster Catalog do not have logs of NS-forming SNe, which are being added for future models, we lump all escaping NSs together without specifying a mechanism. Note, however, that SNe *do* eject the vast majority of NSs in our models.

Also note that the ejection mechanisms are not mutually exclusive. For example, SNe and BH mergers may both take place, sometimes several times, during a single fewbody interaction, each applying separate kicks to their remnants. Via momentum conservation, the other bodies in the interaction receive dynamical kicks in response. For simplicity, however, we ignore this subtlety when classifying the ejection mechanisms of specific escapers. Namely, whenever CMC removes an escaper immediately after a fewbody encounter that also involves SNe or mergers, we count only the direct SNe/merger remnants toward ejection via these secondary mechanisms. All other escapers from the fewbody interaction we attribute to the larger fewbody encounter itself. Our treatment is more precise for *isolated* binaries outside of fewbody. Here, too, an SN may induce an opposite kick to the remnant's companion, ejecting it from the cluster. These escapers we *do* count separately, properly attributing them to either their own SNe or the SNe of their (former) partners.

4. Results

We now examine the properties of escapers at $t_{\rm rmv}$, the time of removal from CMC, when they first satisfy Equation (3). This is prior to any further integration of their trajectories on their way out of the cluster and beyond (see the second paper in this series, N. C. Weatherford et al. 2023, in preparation). Properties of interest include escape mechanism, location and velocity at $t_{\rm rmv}$, escaping star type, and escaping binary properties, such as semimajor axis, eccentricity, and mass ratio. First, however, we briefly demonstrate the overall cluster evolution.

Figure 1 shows the time evolution of our GC simulations, distinguished in line style by Galactocentric distance R_g and in color by virial radius r_v (see legend). Recall that R_g determines a cluster's tidal radius r_t, and r_v its dynamical clock—(Equation (1); GCs with higher R_g have larger tidal boundaries and those with lower r_v (higher density) evolve faster. Together, R_g and r_v also determine how fully a GC fills its tidal boundary, quantifiable by the ratio r_{99}/r_t, where r_{99} is the radius enclosing 99% of the cluster mass. GCs born more tidally filling—i.e., with higher r_v/R_g and r_{99}/r_t—have lower escape speeds in the halo and more easily evaporate. So while low r_v generally hastens escape and cluster expansion (through dynamical heating), low R_g GCs born at high enough r_v can still rapidly disrupt due to their head start in filling their tidal boundaries. This duality is readily apparent in Figure 1. The top two panels show the fractions retained of the initial number of particles $N(t)/N_i$ (left) and total cluster mass $M(t)/M_i$ (right). As expected, GCs with smaller r_v typically evaporate faster for fixed R_g while those with smaller R_g evaporate faster for fixed r_v. But since the evaporation rate depends on both parameters, these individual trends are not always followed; either effect may outweigh the other in certain cases, e.g., for $R_g = 2\,{\rm kpc}$ and $r_v = 4\,{\rm pc}$ (solid yellow). Though the high r_v implies slow relaxation, this model actually evaporates fastest since it is born the most tidally filling, evident from the lower right panel showing r_{99}/r_t.

Finally, the lower left panel shows a rolling average of the theoretical core radius r_c, expressed as a ratio to the half-mass–radius r_h. As expected from their fast dynamics, the GCs with the smallest r_v (0.5 pc; black) reach core collapse earliest—in fact within a Hubble time, demonstrable from their steep drops in r_c/r_h between 8 and 13 Gyr. These drops accompany the transition from a centrally flat to a centrally steep surface

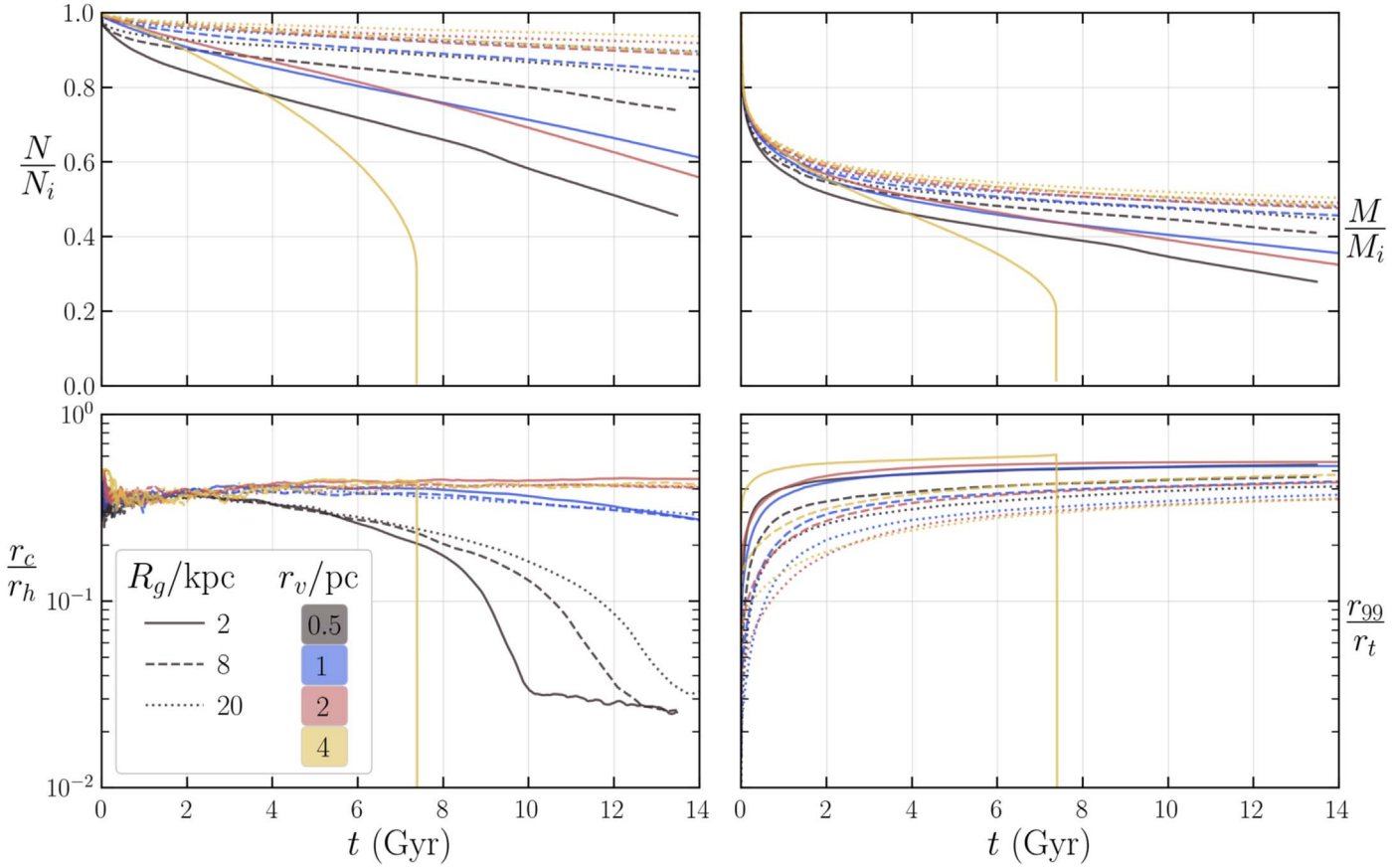

Figure 1. Evolution of cluster models over time. Top left: number of particles relative to the initial number of particles. Top right: cluster mass relative to the initial cluster mass. Bottom left: core radius over half-mass–radius (rolling average). Bottom right: 99% Lagrange radius over tidal radius (rolling average). In all panels, line styles indicate the model's Galactocentric distance while line colors indicate the model's virial radius.

brightness characteristic of an observationally CC'd state (e.g., Kremer et al. 2020, 2021; Rui et al. 2021b).

4.1. Escapers by Escape Mechanism

To examine escape mechanisms in detail, we focus our attention on the CMC models most representative of typical NCC'd and CC'd MWGCs (models 2 and 8 from Table 1, respectively), as measured at a Hubble time under the definitions in Section 1. We record results for all models in the Appendix (Tables A2 and A3). Figure 2 shows the distribution of clustercentric position $r_{\rm rmv}/r_t$ and speed $v_{\rm rmv}/v_{\rm esc}$, as measured at the time of removal $t_{\rm rmv}$ from the NCC'd and CC'd GCs (lower left and central panels, respectively). Here, $v_{\rm esc} = \sqrt{2\alpha\phi(r_t) - 2\phi(r_{\rm rmv})}$ is the escape speed, where $\phi(r)$ is the GC potential and α is the order unity constant defined in Equation (4) to capture the effect of back-scattering. The upper and right corner plots show the corresponding cumulative distribution functions (CDFs) for $r_{\rm rmv}/r_t$ and $v_{\rm rmv}/v_{\rm esc}$ and different colors distinguish the escape mechanisms, as described in the caption and legends. In the corner plots, solid and dashed curves correspond to the NCC'd and CC'd GCs, respectively.

Several reassuring results are evident in Figure 2. First, two-body relaxation (yellow) produces very low-speed escapers with $v_{\rm rmv}/v_{\rm esc}$ barely >1, except very near $r_{\rm rmv}/r_t \sim 1$. Here, $v_{\rm esc}$ is so small that weak encounters can produce $v_{\rm rmv}/v_{\rm esc}$ significantly greater than unity. Furthermore, about half of escapers from relaxation originate within the typical core radius at removal $r_c(t_{\rm rmv})$, indicated by the vertical line and shaded interval in each scatter plot. This echoes the understanding (e.g., Spitzer & Shapiro 1972) that stars near the escape energy in the cluster halo typically evaporate after first plunging back into the core, where the higher density makes relaxation much more efficient.

Also encouraging, the distribution of escapers containing a BH (black) is bimodal, reflecting the dominant two BH ejection scenarios; SNe kicks at modest radial positions of about one core radius and strong encounters in the deep core after formation and further mass segregation. Meanwhile, the overwhelming majority of escapers containing an NS (but no BH) are due to NS SNe kicks, which are stronger than BH SNe kicks, so are distributed at similar position but higher typical speed. Interestingly, the $r_{\rm rmv}$ distributions from both the BH and NS SNe both align very closely with each model's typical $r_c(t_{\rm rmv})$. This reflects that stars massive enough to form either type of compact object ($\approx$20 $M_\odot$ for NSs and $\approx$40 $M_\odot$ for BHs) are proportionately much closer in mass to each other than to typical stars of $\approx$0.5 $M_\odot$, so both mass segregate at roughly the same speed during their progenitors' very short lives. Continued mass segregation of the BHs to the cluster center and ensuing BH burning then forces retained NSs away from the deep core, leaving most of them at roughly the core radius.

More generally, strong encounters dominate escape from the deep core—though not from the core overall since two-body relaxation is so dominant (see, e.g., the escaper counts in the legends used to normalize the $r_{\rm rmv}/r_t$ CDFs at top). Strong

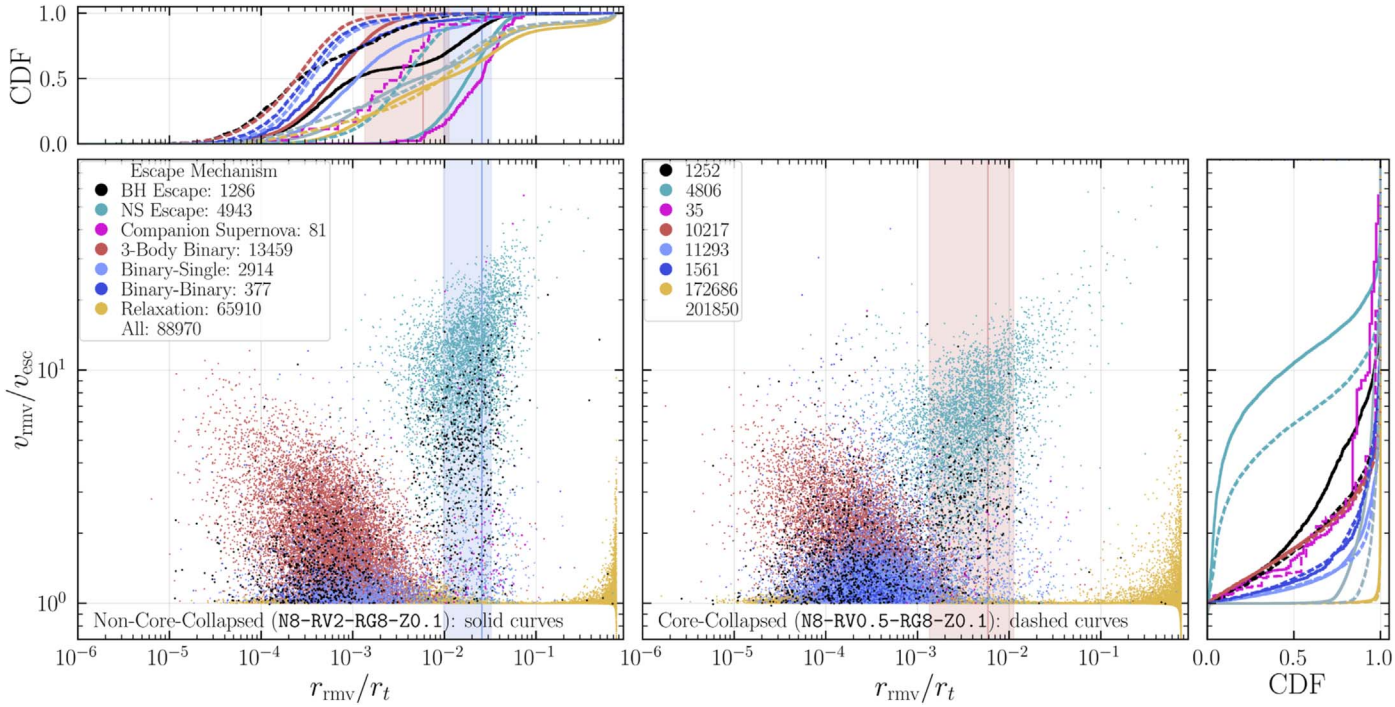

Figure 2. The escapers from the archetypal NCC'd and CC'd cluster models (lower left and central panels, respectively), distributed according to their positions $r_{\rm rmv}/r_t$ and speeds $v_{\rm rmv}/v_{\rm esc}$ at the time of removal from CMC, $t_{\rm rmv}$. The top and right corner plots show the corresponding CDFs for $r_{\rm rmv}/r_t$ and $v_{\rm rmv}/v_{\rm esc}$, respectively, with solid (dashed) curves corresponding to the NCC'd (CC'd) model. In each panel, colors distinguish different escape mechanisms and the gray curves in the CDFs include all escapers. Regardless of escape mechanism, escapers (single or binary) containing a BH are shown in black while escapers containing an NS (but no BH) are shown in teal. All other escapers are categorized as follows: those caused by the induced kick from a binary companion's supernova (magenta), three-body binary formation (red), binary–single (light blue) and binary–binary (dark blue) strong encounters, and two-body relaxation (yellow). The legends also display the total number of escapers and the subtotals from each of the above categories. For each model, the vertical lines and surrounding shaded intervals indicate the median and 10th–90th percentile range of the theoretical density-weighted core radius $r_c(t_{\rm rmv})$ normalized by $r_t(t_{\rm rmv})$. Finally, note the escapers that appear at $r_{\rm rmv}/r_t \sim 1$ to have $v_{\rm rmv}/v_{\rm esc} < 1$ are numerical artifacts. CMC *does* require $v_{\rm rmv} \geqslant v_{\rm esc}$, but the recalculation of the escape energy from CMC output to make this plot in post-processing introduces enough numerical error to shift some escapers with $v_{\rm rmv}/v_{\rm esc} \approx 1$ to $v_{\rm rmv}/v_{\rm esc}$ just barely <1. The effect is small; the median $(v_{\rm esc}-v_{\rm rmv})$ for these escapers is only 2 m s^{-1} while only $\approx$3% of total escapers have $v_{\rm rmv}/v_{\rm esc} < 0.999$.

encounters are especially dominant in the dense core of the CC'd GC (dashed), which also features several times more escapers from binary–single (light blue) and binary–binary (dark blue) interactions, as well as two-body relaxation (though not 3BBF in red, as we will discuss shortly). These reflect the increased density and correspondingly faster dynamics. The $v_{\rm rmv}/v_{\rm esc}$ CDFs from strong encounters (right) are similarly unsurprising; NS SNe kicks are by far the strongest, followed by ejections due to a binary companion's SN (magenta), 3BBF (since forming hard binaries releases much potential energy), and fewbody encounters. Though the difference in median seen in this CDF is small, binary–binary encounters tend to produce slightly higher $v_{\rm rmv}/v_{\rm esc}$ than binary–single encounters, especially in the distribution's high-v tail. This reflects the additional binding energy available to exchange into post-encounter kinetic energy, whether through binary ionization, hardening under exchange, or even triple formation (though they are immediately broken by CMC).

A more surprising result is that three-body binary formation contributes significantly to escape, *especially* to the $v_{\rm rmv}$ distribution's high-speed tail. The latter is expected since 3BBF in CMC produces hard binaries, which exchange more potential energy into orbital speed. (Soft binaries are not considered since they quickly disrupt under weak encounters, anyway.) However, the overall prevalence of 3BBF is unexpected; this mechanism is typically considered a minor contributor to cluster evolution, its impact largely limited to BH binary formation (e.g., Morscher et al. 2013, 2015) and cessation of core collapse in clusters born without binaries—a largely academic scenario (e.g., Heggie & Hut 2003, Ch. 23). As we discuss later in this Section, this undervaluation derives largely from (now outdated) analytic arguments that neglect the extreme impact BHs have on 3BBF. For now, we note that Figure 2 suggests 3BBF is important to escape from GCs, due to its outsize influence on high-speed ejection. Notably, a few tens of 3BBF ejections of luminous stars—more than any other mechanism including companion SNe kicks—occur in the high hundreds of kilometers per second to even $\gtrsim 10^3$ km s^{-1}. This makes 3BBF a possible contributor to *hypervelocity* stars with speeds high enough to escape the MW (for a review, see Brown 2015). Yet while 3BBF dominates cumulative high-speed escape, it is not clear from Figure 2 alone that this dominance applies to present-day MWGCs.

4.1.1. Time Evolution of Escape Mechanisms

To capture the crucial time dependence in the relative strengths of the various escape mechanisms, Figure 3 shows the cumulative number of escapers $N_{\rm esc}$ (top) and escape rate $\Gamma_{\rm esc}$ (bottom) over time, classified by escape mechanism for the NCC'd (left) and CC'd (right) GCs. Mechanisms are separated for escapers containing any BHs (dashed curves) while those containing any NSs (but no BHs) are shown together (solid magenta). Typical stellar escapers, containing no NSs or BHs, are also separated (other solid curves).

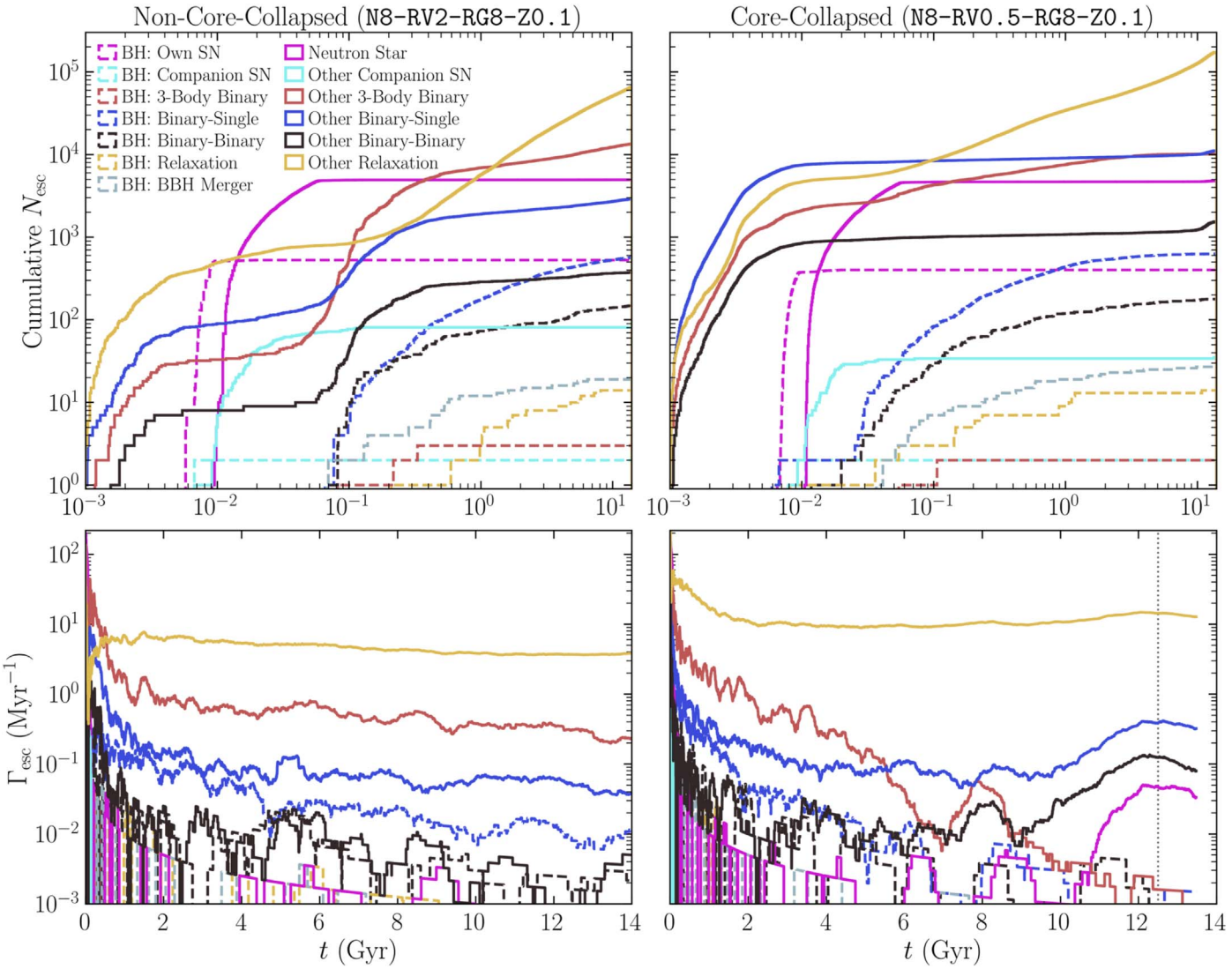

Figure 3. Cumulative number of escapers (upper panels) and rolling average escape rate (lower panels) over time for the archetypal NCC'd and CC'd models (left and right panels, respectively). Note the time axis is logarithmic in the top row but linear in the bottom, to emphasize behavior near present. Escapers containing any BHs (dashed curves) are subdivided by escape mechanism: those ejected by SNe—whether their own (magenta) or a binary companion's (teal)—three-body binary formation (red), binary–single (blue) and binary–binary (black) encounters, binary BH mergers (gray), and two-body relaxation (yellow). Escapers containing any NSs (but no BHs) are shown in solid magenta regardless of escape mechanism (overwhelmingly SNe early on and cumulatively but mostly strong encounters during/after observable core collapse, indicated by the dashed vertical line; see Figure 1). Typical stellar escapers ("other," containing no NSs or BHs) feature in the solid curves, with specific escape mechanisms colored as for the BH escapers. Finally, note the noise floor at $\sim 10^{-3}$ Myr^{-1} (from too small a sample size) in the lower panels decreases slightly as the rolling average window size increases linearly with time, from 1 Myr to 1.4 Gyr.

Two-body relaxation dominates escape and this dominance is especially apparent at late times, i.e., the observable present for MWGCs. (However, note in Table A2 that exactly how much relaxation dominates over strong encounters depends on how tidally filling the GC is. As discussed earlier, tidally filling GCs at low R_g can evaporate much more quickly from relaxation-coupled tides than GCs at high R_g while the strong encounter rate changes little.) Relaxation (solid yellow) contributes $\approx$94% of Γ_{esc} at a Hubble time in the NCC'd GC, followed by 3BBF (solid red; 4%) and binary–single encounters (solid blue; 1%). There is negligible impact from other mechanisms, though some dominate at earlier times; a logarithmic scaling on the lower panels (or especially close look at the upper ones) would reveal that BH SNe (dashed magenta) dominate at $6 \lesssim t/\mathrm{Myr} \lesssim 15$, NS SNe (solid magenta) at $15 \lesssim t/\mathrm{Myr} \lesssim 90$, and other stars via 3BBF at $90 \lesssim t$ Myr$^{-1} \lesssim 500$. Since most BHs escape by a Hubble time, we also see in the upper panels that binary–single strong encounters (dashed blue) and BH SNe each eject close to half of all BHs formed, with <10% ejected by binary–binary encounters and negligible impact from other mechanisms.

There are differences for the CC'd GC (but remember it is simply more dense, so dynamically older; the NCC'd GC would eventually collapse to a similar state if evolved beyond a Hubble time). First, due to the higher initial density, kicks via `fewbody` encounters, 3BBF, and relaxation contribute more to early Γ_{esc}. So neither BH SNe nor 3BBF ever dominate and NS SNe dominate more weakly from 15–100 Myr. Cumulative N_{esc} is also several times higher at all times due to the shorter relaxation timescale. So, unlike ejecta from 3BBF or `fewbody` encounters, which escape at roughly the same rate as in the NCC'd GC by $t \sim 1$ Gyr, escape via relaxation remains faster. Γ_{esc} from `fewbody` encounters and relaxation also peaks once the GC reaches an observably CC'd state (vertical line; see Figure 1). With few BHs

(or NSs) left, the GC enters a phase in which WDs dominate central dynamics and support the core from further collapse via binary WD burning (e.g., Kremer et al. 2021; Rui et al. 2021b; Vitral et al. 2022). $\Gamma_{\rm esc}$ from these mechanisms then returns to gradually decreasing since $r_c(t)$ flattens out while r_h continues to expand from binary burning. So while r_c/r_h in Figure 1 continues contracting (much slower), the GC density and corresponding encounter rates actually decrease.

NS ejections also spike after core collapse, since the absence of BHs allows them to participate more vigorously in the denser central dynamics and eject themselves during `fewbody` interactions correspondingly more often. There are <100 NSs left in the CC'd GC by a Hubble time, so their heightened $\Gamma_{\rm esc}$ (about one NS every 20 Myr) may rapidly deplete their population on a gigayear timescale. However, this outcome neglects possible ongoing NS production through WD–WD mergers (Kremer et al. 2021) and accretion-induced collapse. It is also sensitive to factors controlling the early NS population size, e.g., SN kicks and NS formation through giant collisions and tidal capture (e.g., Ye et al. 2022).

Finally, ejection via 3BBF (solid red) rapidly *falls* during observable core collapse. This is highly counterintuitive since the total 3BBF rate in clusters is $\Gamma_{\rm 3bb} \sim n_s^3$ (or $\Gamma_{\rm 3bb,i} \sim n_s^2$ for any *individual* body), where n_s is the number density of singles. So $\Gamma_{\rm 3bb}$ scales even more steeply with n_s than the total `fewbody` encounter rates—$(\Gamma_{\rm bs}, \Gamma_{\rm bb}) \sim (n_s n_b, n_b n_b) \sim n_s^2$, where n_b is the binary number density—suggesting $\Gamma_{\rm 3bb}$ should also rise during core collapse. This intuition neglects steep dependence on the typical stellar mass m and velocity dispersion σ: $\Gamma_{\rm 3bb,i} \propto n_s^2 m^5 \sigma^{-9}$ (see Equation (7.11) in Binney & Tremaine 2008). $\Gamma_{\rm 3bb,i}$ in `CMC` follows the same scaling, with m the mass of the new binary, and n_s and σ expressed as local averages (for more detail, see Section 2.3.1 Rodriguez et al. 2022, but beware of a typo in their Equation (23); the true `CMC` rate is $1/2$ as large). Crucially, a GC prior to core collapse is in its binary BH burning phase, featuring a robust and dynamically dominant central population of BHs. These BHs are typically 10–20 times more massive than other bodies in the core, so their dominance of central dynamics, including 3BBF, enhances $\Gamma_{\rm 3bb}$ by a factor of $\sim 10^6$ over a first-order approximation based on average *stellar* mass (e.g., Binney & Tremaine 2008). Upon the loss of BHs leading to core collapse, the 3BBF ejection rate craters and even the higher post-collapse density cannot raise it enough to match the earlier BH-driven rate, at least until dynamics eject most remaining *stellar* binaries now responsible for supporting the core.

4.2. A Closer Look at Three-body Binary Formation

The above reasoning is sound; BH mass should increase 3BBF. Yet it still seems to contradict more subtly the findings of Morscher et al. (2013, 2015) that most 3BBF occurs during transient collapses of the central BH population (gravothermal oscillations, *not* observable core collapse). Since BHs are so massive and compact, these transient BH collapses can be significantly deeper than those achieved by stellar bodies (primarily central WDs) after observable core collapse. In other words, the high 3BBF rate during the BH burning phase may not be due to the mass of BHs but rather their capacity to reach extreme densities. Critically, however, Morscher et al. (2013, 2015) only allowed 3BBF to occur between three BHs, greatly limiting $\Gamma_{\rm 3bb}$ overall (e.g., between one BH and two stars). Due to BHs' relative rarity, it is not surprising that 3BBF so constrained would only be efficient during transient collapses of the BH population. To show that our high 3BBF ejection rate $\Gamma_{\rm 3bb}^{\rm ej}$ during the BH burning phase is truly due to the mass of BHs, rather than their ability to collapse to extreme density, we must look more closely at how $\Gamma_{\rm 3bb}$ and $\Gamma_{\rm 3bb}^{\rm ej}$ change with density.

The top row of Figure 4 shows the time evolution of the theoretical core radius r_c and two sets of Lagrange radii enclosing (1%, 10%, 50%) the cluster mass, counting all cluster objects and just those with masses from 10–100 $M_\odot$. Again the NCC'd and CC'd GCs are shown at left and right, respectively. The center row shows the central density and average densities within the above Lagrange radii for all cluster bodies while the bottom row shows the number of BHs in the cluster $N_{\rm BH}$, and 3BBF rates: overall ($\Gamma_{\rm 3bb}$), involving at least one body more massive than 10 $M_\odot$ ($\Gamma_{\rm 3bb}^{>10M_\odot}$), and leading to ejection ($\Gamma_{\rm 3bb}^{\rm ej}$). Though all curves have been smoothed for visibility using a rolling average with a 30 Myr window size, gravothermal oscillations are still easily apparent, with numerous spikes in central density and smaller troughs in the Lagrange radii limited to high masses.

As observed by Morscher et al. (2013), the density peaks (radii troughs) typically occur simultaneously with peaks (troughs) in $\Gamma_{\rm 3bb}$ (blue; though note this is typically obscured by the nearly equal $\Gamma_{\rm 3bb}^{>10M_\odot}$ in red). However, the relative magnitude of these peaks/troughs is not especially consistent; even sharp density spikes often lead to relatively shallow peaks in 3BBF. Thus, much of the 3BBF occurs outside of the BH collapse phases. More tellingly, the CC'd GC features much higher *typical* densities (lower characteristic radii) than the NCC'd GC, due both to its smaller initial r_v and its early core collapse. This remains true of the Lagrange densities of the bodies more massive than 10 $M_\odot$—which are all BHs after the first tens of megayears—and especially so by a Hubble time. Yet even at this point, $\Gamma_{\rm 3bb}$ remains at least a few times higher than in the CC'd GC. So while gravothermal oscillations help induce 3BBF, they are *not* the primary cause of 3BBF overall. $\Gamma_{\rm 3bb}$ instead follows very closely the evolution of $N_{\rm BH}$ (black), leaving BH mass enhancement as the primary cause of 3BBF in our models.

Figure 4 also reveals a couple further interesting nuances to escape via 3BBF. First, $\Gamma_{\rm 3bb}^{>10M_\odot}$ is practically indistinguishable from $\Gamma_{\rm 3bb}$, at least prior to core collapse, demonstrating that almost all 3BBF in the NCC'd GC—and correspondingly, almost all 3BBF-induced ejections—involves at least one BH. Second, Figure 4's lower right panel demonstrates that $\Gamma_{\rm 3bb}^{\rm ej}$ decreases more rapidly with BH loss than $\Gamma_{\rm 3bb}$. So $\Gamma_{\rm 3bb}^{\rm ej}$ is even *more* sensitive to component mass than $\Gamma_{\rm 3bb}$. This is due to momentum conservation in the center-of-mass frame of the three-body interaction, which kicks the binary and single in inverse proportion to their masses. Binaries formed via 3BBF involving a BH will almost always contain the BH (as the most massive object), so these binaries are significantly more massive than those formed in the absence of BHs. They then receive a smaller kick, while the single picks up a larger kick, making its ejection more likely.

4.3. Escaper Demographics

We now examine escaper demographics. For the same two archetypal GCs, the upper three panels of Figure 5 show the cumulative number of escapers over time for different stellar/binary types. Consistent with our earlier look at escape

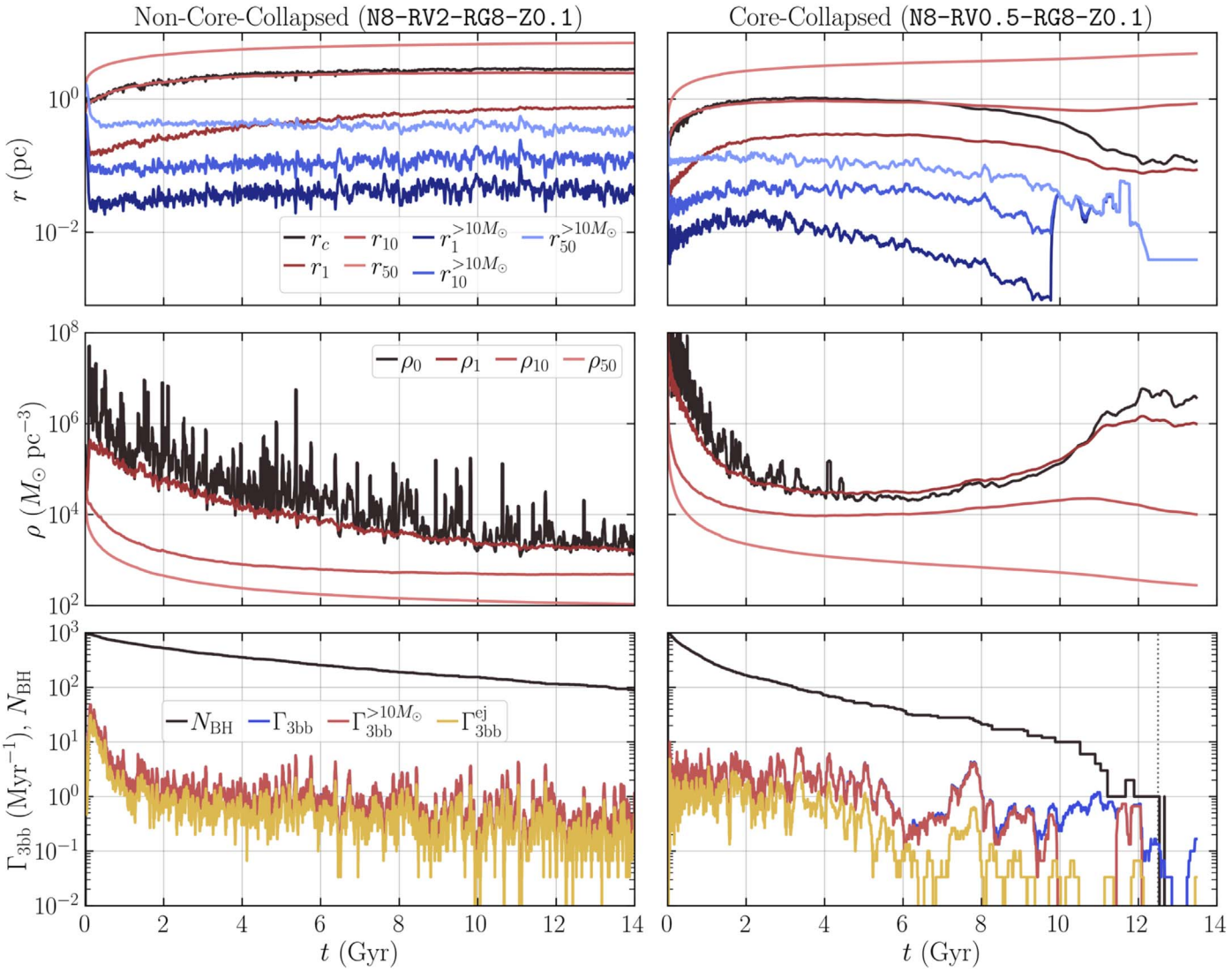

Figure 4. For the archetypal NCC'd and CC'd models (left and right columns, respectively) the upper panels show time-rolling averages of the density-weighted core radius r_c (black; from Casertano & Hut 1985) and Lagrange radii containing (1%, 10%, 50%) of the cluster mass, counting all cluster objects (reds; r_1, r_{10}, r_{50}) and just those with masses $10 < m/M_\odot \leqslant 100$ (blues; $r_1^{>10M_\odot}$, $r_{10}^{>10M_\odot}$, $r_{50}^{>10M_\odot}$). Central panels: time-rolling averages of the density-weighted central density ρ_0 (black; also from Casertano & Hut 1985) and average densities within each the above Lagrange radii counting all cluster objects (reds; ρ_1, ρ_{10}, ρ_{50}). Lower panels: time-rolling averages of the total number of BHs in the cluster N_{BH} (black), the total 3BBF rate Γ_{3bb} (blue), the 3BBF rate involving at least one body with mass $m > 10\,M_\odot$ ($\Gamma_{3bb}^{>10\,M_\odot}$; red), and the ejection rate via 3BBF Γ_{3bb}^{ej} (yellow). Note that $\Gamma_{3bb}^{>10\,M_\odot}$ often obscures Γ_{3bb} due to their near equality at most times. The background grid lines in gray help guide the eye in noticing that many of the peaks/troughs in the 3BBF rates correspond closely in time to peaks/troughs in density (troughs/peaks in radius), yet the relative magnitudes are inconsistent; i.e., large density peaks (radius troughs) do not necessarily lead to large peaks in the 3BBF rates. Finally, the rolling average window size is 30 Myr in all panels.

mechanisms, the top panel shows that in the NCC'd cluster (solid curves), NSs (blue) briefly surpass MS stars (red) as the dominant population from ∼10–100 Myr. At all other times, the MS dominates escape. Due to the CC'd GC's higher density and faster relaxation, more MS stars escape at early times via both strong encounters and relaxation, so NSs never dominate.

The next panel tracks ejection of binaries containing at least one compact object (BH, NS, or WD). Except for BH–BH pairings, the NCC'd GC strongly disfavors ejection of any such binaries. This results from the low initial density and correspondingly low encounter rates, exacerbated by long BH retention; the associated binary BH burning mostly excludes lighter compact objects from the central dynamics. BH–BH binary ejection is only slightly faster in the CC'd GC due to the higher density, but the ejection rates of the other binary species are quite different from the NCC'd case. BH loss precipitating core collapse allows NSs and WDs to participate strongly in central dynamics; tens of ejections each of NS–WD and WD–WD binaries, plus ∼10 NS–MS and nearly 100 WD–MS binaries, occur after the steepest phase of core contraction around 10 Gyr (see Figure 1's dashed black curve).[7]

The third panel shows the time-rolling average mass of escaping binaries (blue) and singles (black). There is a large peak for binaries in the first couple gigayears due to frequent ejection of BH binaries through hardening encounters with

[7] Curiously, ∼10 each of NS–WD and WD–MS binary ejections occur far earlier in the NCC'd GC, a result that should be viewed skeptically. These few are almost all primordial binaries and feature initial mass ratios near unity and significant mass transfer (especially the NS–WDs). Their prompt ejection from the NCC'd model but not the denser CC'd model likely arises from a CMC prescription that scales the initial semimajor axis linearly with r_v. This causes the CC'd GCs to start with harder binaries, which may then be more susceptible to mass transfer instabilities in stellar evolution with BSE.

other bodies. This peak is significantly smaller for the CC'd cluster because several times more binaries overall are ejected via faster dynamics, while the number of BH binary ejections is roughly the same due to their limited supply (see the second panel). In both clusters by a Hubble time, the average mass of single ejections is $\approx 0.3\,M_\odot$ (binary masses $\approx 0.5\,M_\odot$ in the CC'd GC and $\approx 0.8\,M_\odot$ in the NCC'd GC). This is about 50% less than the average stellar mass in the cluster, reflecting the preferential ejection of low-mass stars due to their lower inertia.

The lowest panel compares time-rolling averages of the binary fractions in the cluster overall (gray), within its theoretical core radius (black), among all escapers (blue), and among stellar relaxation-induced escapers only (yellow). The overall cluster binary fraction f_b is nearly constant, decreasing only slightly over a Hubble time due to dynamical destruction of binaries through strong encounters and collisions (e.g., Hurley et al. 2007; Chatterjee et al. 2010). In contrast, the binary fraction in the core ($f_{b,c}$) increases due to mass segregation, and does so much faster in the CC'd GC (see Chatterjee et al. 2010), due to its faster relaxation. Since relaxation-induced escape primarily takes place in the core (e.g., Figure 2), one might expect the binary fraction among *only* relaxation-induced escapers ($f_{b,\mathrm{relesc}}$) to trace $f_{b,c}$—or at least somewhere in between $f_{b,c}$ and f_b overall. Yet $f_{b,\mathrm{relesc}}$ is nearly identical in both GCs and noticeably lower than $f_{b,c}$ or f_b. This reflects the higher mass of binaries relative to singles; momentum conservation during weak encounters with singles then causes binaries to receive smaller kicks. This may damp the escaper binary fraction (relative to $f_{b,c}$) more in the CC'd GC since the faster dynamics allows for more binary exchange interactions, which tend to increase component mass. Finally, due to the dominance of relaxation-induced escape, it is unsurprising that the *overall* escaper binary fraction $f_{b,\mathrm{esc}}$ closely tracks $f_{b,\mathrm{relesc}}$ from relaxation only. Less obviously, $f_{b,\mathrm{esc}}/f_{b,\mathrm{relesc}}$ is slightly higher in the CC'd GC since its higher density generates more strong `fewbody` encounters, which feature higher kicks.

4.4. Escaping Binaries

More detailed properties of binary escapers merit further examination. Figure 6 shows the distributions in semimajor axis (a; CDF at upper left), eccentricity (e; CDF at center right), and secondary-to-primary mass ratio (q; CDF at lower right) among all escapers from the NCC'd and CC'd GCs (solid and dashed curves, respectively). The four scatter plots show the two-dimensional shape of these distributions for each cluster (NCC'd in the lower left pair of panels and CC'd in the central pair). Different colors correspond to different binary types, as described in the caption. It is readily apparent in the top panel that binaries escaping from the CC'd GC have smaller a than binaries in the NCC'd GC, due to faster dynamics (faster hardening) and the higher central escape speed (allowing for more hardening before ejection).

In both GCs, the eccentricities of ejected BH–BH binaries (black) are nearly thermal, as expected for binaries in statistical equilibrium (e.g., Jeans 1919; Ambartsumian 1937; Heggie 1975). Meanwhile, ejected binaries overall (yellow) strongly disfavor high e—as do in-cluster binaries at late times, not shown—consistent with surveys of the Galactic field (for recent reviews, see, e.g., Duchêne & Kraus 2013; Moe & Di Stefano 2017). Since many field stars likely escaped from disrupted star clusters (e.g., Lada & Lada 2003), the result that stellar escapers from `CMC` have a similarly flat e distribution is encouraging. However, it is also somewhat counterintuitive theoretically, since dynamically formed binaries tend to have thermal eccentricities (Heggie 1975) and `CMC` correspondingly draws e from a thermal distribution for both primordial binaries *and* those generated via 3BBF.

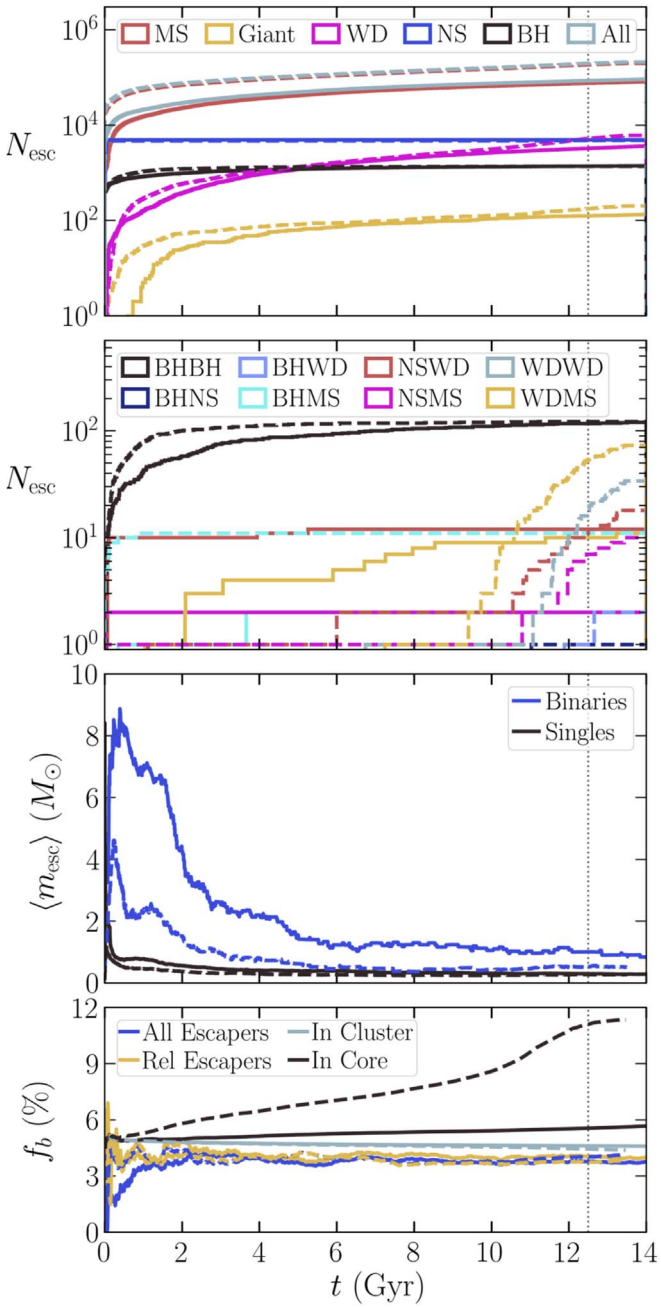

Figure 5. Top two panels: cumulative number of escapers over time for the archetypal NCC'd and CC'd models (solid and dashed curves, respectively). The top panel tracks all escaping bodies by stellar type (binary components count individually); MS = main-sequence, WD = white dwarf, NS = neutron star, BH = black hole, and "Giant" includes stars in the Hertzsprung gap. The second panel tracks binaries containing at least one compact object. Note there are no such ejecta with Giant companions. Third panel: Time-rolling average mass of escaping bodies. Bottom panel: time-rolling average binary fractions in the cluster overall (gray), within the cluster's density-weighted core radius (black), among all escapers (blue), and among stellar relaxation-induced escapers only (yellow). In all panels, the vertical line indicates the onset of WD binary burning (observational core collapse, see Figure 1).

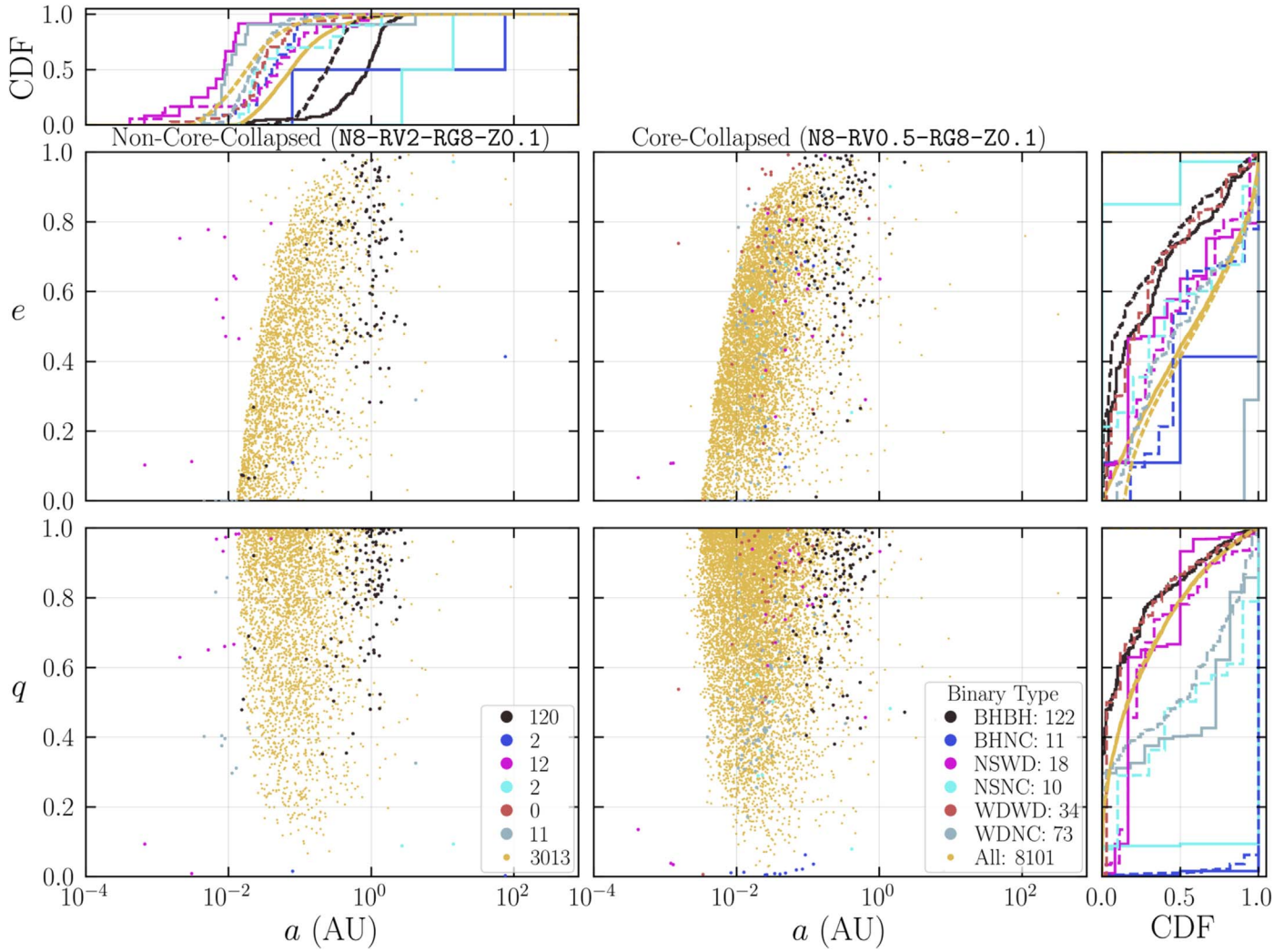

Figure 6. Properties of escaping binaries from the archetypal NCC'd and CC'd models (left and central scatter plots, respectively), distributed according to their eccentricity e, mass ratio $q = m_{\rm secondary}/m_{\rm primary}$, and semimajor axis a, all at the time of removal $t_{\rm rmv}$ from CMC. In clockwise order, the top and rightmost corner plots show the corresponding CDFs for a, e, and q, respectively, with solid (dashed) curves corresponding to the NCC'd (CC'd) model. In each panel, colors distinguish several types of binaries: BH–BH (black), BH–NC (blue), NS–WD (magenta), NS–NC (teal), WD–WD (red), WD–NC (gray), and all binaries (yellow). Here, "NC" indicates when one of the binary components is *non-compact*, i.e., any body (overwhelmingly MS stars) other than a WD, NS, or BH. For each model, the legends in the lower panels also display the total number of binary escapers and the subtotals from each of the above categories.

This tension echoes the finding of Geller et al. (2019) that clusters—simulated with both CMC and direct N-body codes—cannot thermalize initially uniform/near-uniform e distributions in MS stars, even after several Hubble times. (In our case, the tension is worse because the primordial binaries start thermal and actively become less so for both in-cluster and ejected binaries.) This counterintuitive result arises from a couple factors. First, while frequent strong scattering encounters can increase e, high e also translates to shorter pericenter distances and correspondingly more stellar collisions, destroying binaries that grow too eccentric. Less extremely, small pericenter can lead to mass transfer, common envelope, and strong tides in binary stellar evolution. As dissipative processes, these circularize e. Hard binaries dynamically ejected from the dense core can be subject to these processes for extended periods with few interruptions from e-enhancing encounters.

The clusters' binary mass ratios $q = m_{\rm secondary}/m_{\rm primary}$ are also similar. Escaping binaries overall exhibit a strong tendency toward $q \sim 1$, especially for BH–BH binaries, though some pairings intuitively exhibit $q \ll 1$—e.g., BH–NC binaries (blue) between a BH and any *non-compact* object (overwhelmingly MS stars). In fact, the overall q distribution for escapers is very similar to that for in cluster binaries at a Hubble time (not shown), with only a slightly higher skew toward $q \sim 1$. So the q distribution predominantly reflects strong fewbody dynamics in GCs, in which binaries preferentially swap in companions of higher mass (e.g., Heggie & Hut 2003, Ch. 19). While the most massive objects in old GCs are BHs, followed distantly by NSs and massive WDs, the upper end of the MS remains by far the most numerous massive population, so binaries in GCs generally favor MS–MS binaries with both component masses near the MS turnoff, i.e., a mass ratio $q \sim 1$. This is qualitatively consistent with binaries surveyed in MWGCs, characterized by a roughly uniform mass ratio for $q \lesssim 0.9$ with a sharp over-density for $q \gtrsim 0.9$ (Milone et al. 2012). In contrast, binaries in the Galactic field generally exhibit more asymmetric mass ratios (e.g., Moe & Di Stefano 2017). So the tendency toward $q \sim 1$ in binaries escaping from GCs could help in identifying field binaries with origins in nearby MWGCs. However, this should

only be leveraged as a supplement to more robust signals, e.g., proper motion, position, and metallicity.

Finally, we find that even in the CC'd GC, most binaries (>80%) escape via two-body relaxation, with binary–binary strong encounters contributing most of the rest. Binary–single encounters eject only a small fraction of binary escapers ($\lesssim$5% each). In CMC, 3BBF almost never ejects the binary (twice throughout all 12 simulations analyzed). This occurs since 3BBF is by far more efficient when a BH (massive body) is involved. Consequently, the typical binary-to-single mass ratio at the end of a 3BBF encounter in CMC is $\sim$10. To conserve momentum in the encounter's center-of-mass frame, the binary thus receives a much smaller recoil kick than the single.

5. Discussion

Before summarizing our findings and future work, we now discuss the surprising impact of three-body binary formation on escape from GCs and limitations to our analysis.

5.1. Relevance of Three-body Binary Formation

We find three-body binary formation occurs often enough in GCs to cumulatively power many high-speed ejections in the NCC'd GCs typical of the MW but *not* GCs that are observably CC'd (i.e., with steep central surface brightness). This finding completely reverses common arguments that 3BBF is negligible until *after* core collapse, especially given similar doubts about its dynamical impact even then. These arguments rest on flawed assumptions while the apparent reversal in behavior relative to *core collapse* stems from evolution in usage of the term.

First, analytic estimates of the 3BBF rate (e.g., Heggie 1975; Goodman & Hut 1993; Binney & Tremaine 2008) have sometimes been misinterpreted, in conjunction with a low assumed stellar mass, to suggest the rate is negligible prior to core collapse (e.g., Hut 1985; Freitag & Benz 2001; Joshi et al. 2001), or even thereafter (e.g., Statler et al. 1987; Hut et al. 1992). Such studies generally predate the cluster modeling community's widespread incorporation of primordial binaries and realistic IMFs—and thereby the modern consensus that GCs retain robust BH populations prior to collapse. As noted in Section 4.1, BHs greatly enhance 3BBF due to the 3BBF rate's steep mass dependence (see also Kulkarni et al. 1993; O'Leary et al. 2006; Banerjee et al. 2010; Morscher et al. 2013, 2015). Without such massive bodies, efficient 3BBF would indeed require extreme cluster density only achieved in deep core collapse. Additionally, binary burning prevents modern GC models with primordial binaries from reaching such extremes (e.g., Goodman & Hut 1989). Modern usage of the term *core collapse* has changed accordingly and is not limited to such deep collapse halted by 3BBF. Rather, as in this study, it often refers to the core contraction arising from BH ejections, which transition the core from binary BH burning to weaker binary WD burning, as described in Section 1. The lower mass of WDs causes the 3BBF ejection rate to drop precipitously due to the overall 3BBF rate's steep mass dependence, made even steeper by the extra mass dependence in the leftover single's speed (via momentum conservation), as discussed in Section 4.2. This overwhelms the boost from higher density post-collapse. Only once strong encounters harden and eject the remaining binaries can deeper collapse occur. The combination of the above factors—neglect of BH populations and updated terminology—explain the apparent reversal in 3BBF's behavior in relation to core collapse.

Second, binaries formed via 3BBF that are especially soft or especially hard do not survive long enough to contribute much to binary burning. In the former case, strong encounters quickly disrupt the binary, while in the latter they harden it until the components eventually merge, if they are not ejected from the cluster first (e.g., Hut & Inagaki 1985; McMillan 1986; Goodman & Hernquist 1991; Bacon et al. 1996; Chernoff & Huang 1996; Fregeau et al. 2004). This reasoning has previously been used to justify neglecting 3BBF in CMC, either entirely (e.g., Joshi et al. 2000; Fregeau et al. 2003) or if any of the bodies is not a BH (e.g., Morscher et al. 2015). Unfortunately, this neglects formation of binaries more intermediate in hardness that survive long enough to contribute substantially to binary burning, as well as 3BBF of BHs with non-BHs. Binary survival is also entirely irrelevant to 3BBF's impact on the escape process; formation of even a short-lived binary in a three-body encounter still kicks the third body. 3BBF can therefore contribute significantly to cluster dynamics via both binary burning and ejection.

Our findings are susceptible to inaccuracies, too, however, especially since CMC uses an approximate recipe (Rodriguez et al. 2022, and references therein) for 3BBF rather than direct integration with, e.g., `fewbody`. In brief, CMC divides a radially sorted list of all singles in the GC into sets of three and computes the 3BBF probability for a binary with a certain minimum hardness based on the three masses and local average relative velocity and number density. The prescription in CMC automatically pairs the two most massive bodies in a set to form a binary. Realistically, this may be the most likely pairing but is not guaranteed. This skews the mean mass ratio between the binary and leftover single to be $m_b/m_s \sim 10$, making immediate ejection of the binary from the GC exceptionally difficult as the ratio of the final speeds in the 3BB interaction's center-of-mass frame is $v_b/v_s = m_s/m_b \sim 0.1$. This sensitivity to the mass ratio means automatic pairing of the two most massive bodies may bias the ejection speeds.

CMC's 3BBF recipe also samples eccentricity e from a thermal distribution for all values of semimajor axis a, but scattering experiments show $\langle e \rangle$ increases with a and is higher than thermal even at the hardest a tested ($1/2$ the hard-soft boundary; Aarseth & Heggie 1976). CMC further assumes the probability P of binary formation is 100% when the three bodies all pass within a region of size a, though the tests show $P \approx 54\%$ for a at the hard-soft boundary. Notably, Aarseth & Heggie (1976) only studied the case of equal masses. So while Morscher et al. (2013) found good agreement between 3BBF rates from CMC and direct N-body methods, the above uncertainties in light of 3BBF's dominance of high-speed ejections suggest that upgrading the 3BBF recipe to use `fewbody` may be highly worthwhile.

5.2. Additional Limitations

Our analysis is subject to several further limitations in addition to those affecting three-body binary formation. Some were previously noted in Section 3.2, but we recap them here with an emphasis on how they may affect the results, as well as options to address them in the future.

First, and most generally important to escape physics, CMC assumes spherical symmetry and therefore is not reliable close to the tidal boundary. Fortunately, however, even two-body

relaxation mostly ejects bodies from the cluster core, where the true tidal potential is still very spherical (e.g., Section 4.1 and Spitzer & Shapiro 1972). So spherical symmetry matters less given our focus on escape mechanisms rather than escape trajectories. (Direct integration of escaper trajectories from the point they first meet the energy criterion mitigates this limitation in follow-up work.)

Second, CMC neglects time-dependent external tides from eccentric or disk-crossing GC orbits, including disk and bulge shocking, which would cause the evaporation rate in Figure 3 to fluctuate and increase overall. The Monte Carlo cluster modeling method can accommodate tidal shock heating(e.g., Spitzer & Chevalier 1973; Spitzer & Shull 1975). However, the method's faster Hénon-style variant used in most modern implementations (including CMC) is not ideally suited for this, being an orbit-averaged approach; rather than evolving each body's orbit on the crossing timescale, it averages over the effects on the (much longer) relaxation timescale. Since tidal shocks occur on the crossing timescale, codes like CMC can only approximate these processes. Yet work on implementing such prescriptions into CMC is in progress (see also discussion in Rodriguez et al. 2023).

Third, while CMC can and does form IMBHs of several hundred solar mass in certain circumstances (see, e.g., González et al. 2021; Weatherford et al. 2021; González Prieto et al. 2022), the code cannot yet fully model the influence of an off-center IMBH in the range 10^3–$10^4\,M_\odot$. Efforts are underway to add this capability, but for the time being, CMC cannot explore the dynamical effects of truly massive BHs in GCs. As discussed in Section 2.2.3, the presence of such a massive body in any GC could significantly increase the rate of high-speed ejections from the cluster. Hence, future analysis of IMBH-induced ejections in full GC models—whether direct *N*-body or Monte Carlo codes—may help constrain the possible presence of IMBHs in GCs with well-measured ejection speed distributions (e.g., Šubr et al. 2019).

On a lesser note, CMC does not consider strong two-body encounters, which may slightly increase the ejection rate at intermediate speeds up to several times the local escape speed. CMC can be upgraded to do so by passing some two-body encounters to `fewbody` instead of the main relaxation algorithm; while the overall effect of such a change is likely minimal due to the rarity of such encounters, it may be worthwhile given the relative ease of such an upgrade. It is also a direct first step to a more complex (and likely more impactful) `fewbody`-based implementation of three-body binary formation.

Finally, CMC does not yet feature asymmetric mass ejection during physical collisions, tidal capture, or tidal disruption events. Consideration of kicks due to asymmetric mass loss during these phenomena may have important effects on the upper end of the ejection speed distribution and the presence of exotica, such as stripped stars in the outskirts of GCs. Note this includes tidal tails and stellar streams—which primarily channel low-speed escapers—since kicks due to asymmetric mass loss from these events may be quite modest (Section 2.2.2). These considerations may be more important for observably CC'd GCs, given their higher collision and tidal disruption rates. The severe shortage of BHs in these GCs would also heighten the impact of collisions and disruptions involving NSs/WDs at the expense of those involving BHs. For these reasons, improvement of CMC's collision and tidal disruption prescriptions, grounded in hydrodynamical simulations, is an ongoing priority (e.g., Kıroğlu et al. 2022; Kremer et al. 2022a, 2022b; Ye et al. 2022).

6. Summary and Future Work

The Gaia telescope has revealed numerous stellar streams and traced the origin of several to specific MWGCs. This connection and the streams' importance to Galactic archeology highlight the need for further examination of escape from GCs. As a first step toward a detailed comparison of the ejecta from our CMC models to extra-tidal stellar populations from the Gaia survey in the vicinity of MWGCs, we have studied escape mechanisms in CMC. Consistent with long-standing theory (e.g., Spitzer & Shapiro 1972) and numerical modeling (e.g., Perets & Šubr 2012; Moyano Loyola & Hurley 2013), we find that two-body relaxation in the cluster core dominates the overall escape rate while central strong encounters involving binaries contribute especially high-speed ejections, as do SNe and GW-driven mergers. We also find the escape rate at a Hubble time in observably CC'd clusters reflects the transition from binary BH burning to binary WD burning (Kremer et al. 2021), boosting late ejections of WD and NS binaries.

We have also shown for the first time that three-body binary formation plays a significant role in the escape dynamics of NCC'd GCs typical of those in the MW. BHs are an essential catalyst for this process due to the 3BBF rate's sensitive dependence on binary mass. As long as a significant BH population remains in the cluster's core, 3BBF dominates the rate of present-day high-speed ejections over any other mechanism, including standard binary–single and binary–binary scattering interactions. This includes production of hypervelocity stars with speeds in the hundreds of kilometers per second to even $\gtrsim 10^3$ km s^{-1}. 3BBF then plummets with the loss of BHs at the onset of observable core collapse.

Except for BH–BH binaries, we find that binary escapers from GCs (as well as in-cluster binaries at late times) are far more circular than expected from a thermal distribution, consistent with observations of the Galactic field (e.g., Moe & Di Stefano 2017). This occurs even though CMC's initial binary eccentricities are thermal, including for those produced via 3BBF. This echoes Geller et al. (2019), who found that since dynamical hardening and collisions deplete eccentric binaries, realistic cluster dynamics do not necessarily thermalize initially uniform eccentricities, contrary to arguments based on thermal equilibrium. Our findings go a step further by demonstrating that dynamics actively de-thermalize the eccentricity distribution, which motivates drawing initial eccentricities in future modeling from flatter distributions more consistent with observations.

Finally, while this study provides a broad sense of the escape mechanisms and demographics of escapers from GCs, the results are not immediately comparable to Gaia observations. In our next work (N. C. Weatherford et al. 2023, in preparation), we therefore integrate the trajectories of CMC escapers in a full Galactic potential and continue their internal stellar evolution to construct realistic velocity distributions in the extra-tidal regions of CMC models and mock surface brightness profiles (in the Gaia bands) extending out to several tidal radii. We will explore how well this post-processing approach reproduces tidal tails, currently unclear due to CMC's assumed spherical symmetry. In later work (N. C. Weatherford et al. 2024, in preparation), we will identify likely past members (*extra-tidal*

candidates) of specific MWGCs and directly compare the mock ejecta from our cluster models to the Gaia data. As shown recently by Grondin et al. (2023), combining precise astrometry with chemical tagging is an especially promising method of identifying such extra-tidal ejecta, and may even be used to identify stars from particular ejection mechanisms. Ultimately, we hope to better understand stellar stream formation and, in an ideal case, leverage the new observables from Gaia to better constrain uncertain properties about MWGCs such as stellar BH or IMBH content, SNe kicks, and the initial mass function, which affect ejection velocities and the cluster evaporation rate.

This work was supported by NSF grant AST-2108624 and NASA grant 80NSSC22K0722, as well as the computational resources and staff contributions provided for the Quest high-performance computing facility at Northwestern University. Quest is jointly supported by the Office of the Provost, the Office for Research, and Northwestern University Information Technology. G.F. and F.A.R. acknowledge support from NASA grant 80NSSC21K1722. N.C.W acknowledges support from the CIERA Riedel Family Graduate Fellowship. F.K. acknowledges support from a CIERA Board of Visitors Graduate Fellowship. S.C. acknowledges support from the Department of Atomic Energy, Government of India, under project No. 12-R&D-TFR-5.02-0200 and RTI 4002. K.K. is supported by an NSF Astronomy and Astrophysics Postdoctoral Fellowship under award AST-2001751.

Software: CMC (Joshi et al. 2000, 2001; Fregeau et al. 2003; Fregeau & Rasio 2007; Chatterjee et al. 2010; Morscher et al. 2013; Pattabiraman et al. 2013; Rodriguez et al. 2021, 2022), fewbody (Fregeau et al. 2004; Antognini et al. 2014; Amaro-Seoane & Chen 2016), SSE/BSE (Hurley et al. 2000, 2002), matplotlib (Hunter 2007), NumPy (Harris et al. 2020), SciPy (Virtanen et al. 2020), pandas (Reback et al. 2022), Astropy (Astropy Collaboration et al. 2013).

Appendix
Escape Criteria and the Tidal Boundary

Formally defining membership in, and escape from, star clusters is conceptually simple but practically challenging. There are theoretical and modeling nuances that while not discussed above for brevity remain worthy of mention. We begin by reviewing the theoretical energy criterion for escape (Appendix A.1) before discussing some subtle inconsistencies in the criteria used in cluster modeling (Appendix A.2). Finally, we include several supplementary tables. Specifically, Table A1 summarizes the current and planned near-future utilization of escape mechanisms in CMC; Table A2 lists for each model the cumulative counts of escapers by escape mechanism; and Table A3 lists for each model the cumulative counts of escapers by stellar and binary type.

A.1. Theoretical Energy Criterion

Star clusters experience a purely static tide in the limit that they circularly orbit within the disk of a radially symmetric galaxy. The motion of objects much less massive than the total cluster mass M_C or galactic mass M_G enclosed by this orbit are the familiar domain of the circular, restricted three-body problem. In this case, the sum of the cluster and galactic potentials—$\phi_c(r)$ and $\phi_g(r)$, respectively—is static in the frame rotating with the cluster at angular velocity $\Omega = \Omega\hat{z}$, where r measures from the center of mass between the cluster and galaxy and $\hat{z}$ is perpendicular to the orbital plane. When neglecting internal gravitational scattering between cluster members, the Jacobi integral E_J is conserved for each object in this frame (see Binney & Tremaine 2008):

$$E_J = \frac{v^2}{2} + \phi_c(r) + \phi_g(r) - \frac{\Omega^2}{2}(x^2 + y^2). \tag{A1}$$

The sum of the last three terms on the right is the effective potential $\phi_{\rm eff}$. Since $v^2 > 0$, Equation (A1) implies that objects cannot enter regions where $\phi_{\rm eff} > E_J$. The Jacobi–Hill surfaces defined by $\phi_{\rm eff} = E_J$ range from fully and separately enclosing the cluster and galactic center (highly negative E_J) to allowing passage through narrow openings directly toward and away from the galactic center (modestly negative E_J), to disappearing entirely (high E_J, excluding no regions).

The highest-E_J surface still *fully enclosing* the cluster is the football-shaped Roche surface familiar from binary evolution, whose ends terminate at saddle points of $\phi_{\rm eff}(r)$ known as Lagrange points, where $\nabla\phi_{\rm eff}(r) = 0$. So, by definition, objects within the cluster may only cross beyond the Roche surface once they have $E_J > \phi_{\rm eff}(r_J)$, where the Jacobi radius r_J is the distance between the cluster and either Lagrange point. Solving $\nabla\phi_{\rm eff}(r) = 0$ in the limit $\mu = M_C/M_G \ll 1$ for a cluster and galaxy that are both point masses results in the expression (e.g., Binney & Tremaine 2008) $r_J/R_G \approx (\mu/3)^{1/3}$. This result changes negligibly for more realistic cluster potentials, so long as $\nabla\phi_c(r_J)$ is small, i.e., when the half-mass–radius r_h enclosing half the cluster mass satisfies $r_h/r_J \ll 1$. However, r_J does change significantly for more realistic galactic potentials since much of a galaxy's mass lies beyond the orbit of a typical star cluster ($R_G \sim 10$ kpc in the MW) and so $\nabla\phi_g(r_J)$ remains steep. A logarithmic MW potential based on the r^{-2} scaling of the MW mass density increases the Jacobi radius to $r_J/R_G \approx (\mu/2)^{1/3}$ (e.g., Spitzer 1987).

Since objects within the cluster may only cross beyond the Roche surface once they have $E_J > \phi_{\rm eff}(r_J)$, r_J is a common choice for the definition of a sphericalized *tidal radius* and the criterion for escape beyond this radius is simply

$$E_J > \phi_{\rm eff}(r_J) \approx -\frac{3}{2}\frac{GM_C}{r_J}, \tag{A2}$$

where the second equality holds for either definition of r_J above —e.g., Equation (5.6) in Spitzer (1987). This criterion is necessary but not sufficient for objects to cross beyond r_J since r_J is the *maximum* distance to the (nonspherical) Roche surface; the *minimum* distance is actually $\approx 2r_J/3$ in the $\hat{y}$-direction parallel to the cluster's velocity. As pointed out by Spitzer (1987), this introduces potential inconsistency between r_J and an observational tidal boundary $r_{t,\rm obs}$, typically extrapolated from the surface density in regions where the equipotential surfaces are still quite spherical. The observed values of $r_{t,\rm obs}$ should in principle include this 2/3 factor: $r_{t,\rm obs} \equiv 2r_J/3$. Ultimately, the exact definition of an inherently approximate tidal radius is somewhat arbitrary and further alternatives exist, such as a more intermediate value $2r_J/3 < r_{t,\rm vol} < r_J$ defined to enclose a spherical volume equal to that enclosed within the actual (nonspherical) Roche surface.

The escape criterion and cluster membership determined by the tidal boundary are nebulous for other reasons, as well. For

Table A1
List of Escape Mechanisms and Status in CMC

	Mechanism Type	Mechanism	Implementation	Status in CMC
Evaporation	Two-body relaxation with static tides	Two-body relaxation	ACTIVE	Toggleable ON/OFF; adjustable Coulomb logarithm (default 0.01) and max. deflection angle (default $\sqrt{2}$).
		Static galactic tide	ACTIVE	Toggleable ON/OFF; circular cluster orbit in logarithmic Galactic potential with adjustable circular velocity (220 km s^{-1}).
	Time-dependent tides	Elliptical/inclined orbit	OPTIONAL	Partially toggleable ON/OFF by providing at simulation start a data table describing a time-varying tidal tensor.
		Tidal shocking	⋯	Implementation under consideration, but is challenging since CMC operates on the relaxation timescale while shocks can operate on the crossing timescale.
Ejection	Strong encounters	Strong two-body encounters	⋯	Implementation with fewbody likely by 2024.
		Three-body binary formation	ACTIVE	Toggleable ON/OFF (for all bodies, just BHs, or none at all) semi-analytic prescription (Morscher et al. 2013); can set minimum hardness ratio (default $\eta = 1$). Upgraded implementation with fewbody possible by 2024.
		Binary–single	ACTIVE	Toggleable ON/OFF.
		Binary–binary	ACTIVE	Toggleable ON/OFF.
		Higher-order encounters	⋯	Implementation possible but largely unwarranted (probably only relevant in very dense young clusters).
		Unstable triple disintegration	PARTIAL	Not toggleable; CMC breaks apart and records all formed triples at birth.
	(Near-)contact recoil	Direct physical collisions	PARTIAL	Toggleable ON/OFF; idealized sticky-sphere prescription without asymmetric mass loss makes this not yet a true ejection mechanism.
		TDEs	⋯	None so far; while TDE rates have been studied with CMC in post-processing, prescriptions to modify stars as a TDE occurs are under active development.
		GW-driven mergers	ACTIVE	Toggleable ON/OFF; post-Newtonian terms included in CMC's fewbody integrator.
	Stellar evolution recoil	BH SNe kicks	ACTIVE	Adjustable prescription; see text and/or Kremer et al. (2020).
		NS SNe kicks	ACTIVE	Adjustable prescription; see text and/or Kremer et al. (2020).
		WD kicks	⋯	Not currently implemented, though uniform 2–9 km s^{-1} kicks were tested in a past CMC version (Fregeau et al. 2009).

Table A2
Cumulative Counts of Escapers by Type and Escape Mechanism

	Escapers with BH(s)							With NS(s)	Without BHs or NSs				
	BBH Merger (1)	Own SN (2)	Comp. SN (3)	3BB (4)	BS (5)	BB (6)	Relax. (7)	(8)	Comp. SN (9)	3BB (10)	BS (11)	BB (12)	Relax. (13)
1	29	417	5	1	640	183	12	4945	25	9753	11,783	1551	397,922
2	27	401	2	2	628	178	14	4806	35	10,217	11,293	1561	172,686
3	35	418	3	0	628	189	10	4732	22	10,763	9225	1216	110,691
4	33	498	7	0	625	171	13	4872	50	12,625	3397	427	286,870
5	30	487	4	3	604	208	9	4812	44	13,598	3234	444	101,547
6	34	486	5	4	601	194	8	4829	48	13,266	3450	432	58,592
7	17	532	2	1	540	177	20	4998	84	14,142	3216	439	328,236
8	19	528	2	3	572	148	14	4943	81	13,459	2914	377	65,910
9	15	530	4	2	527	165	12	4955	78	14,031	3026	436	40,859
10*	5	560	6	5	337	137	56	5101	93	10,568	3588	605	772,543
11	10	550	5	6	402	152	14	5026	93	14,162	3461	581	59,361
12	14	551	9	4	392	136	13	5007	92	12,370	2867	450	28,036

Note. The number of escapers (singles or binaries) containing at least one BH (1–7), at least one NS but no BH (8), and everything else (neither NSs nor BHs; 9–13). The first and third of these categories are further divided by escape mechanism: a binary BH merger kick (1), the escaper's own SNe (2), a (former) binary companion's SN (3), three-body binary formation (4, 10), a binary–single `fewbody` encounter (5), (11), a binary–binary `fewbody` encounter (6, 12), and two-body relaxation (7, 13). The * on simulation 10 indicates that the values are not entirely reliable since the cluster fully disrupted and the final totals therefore include late-stage evolution on a dynamical timescale, which `CMC` cannot accurately capture.

instance, escape under the above condition is reversible; even once a body's E_J is sufficient to allow its escape from the cluster—at which instant it is technically unbound, i.e., a *potential escaper*—gravitational interactions with other bodies on its way out of the cluster can scatter it back down to lower energy. Such back-scattering is a long-known complication to cluster escape (e.g., Chandrasekhar 1942; King 1959). This means that some significant fraction of unbound particles within the Roche surface at any particular instant will become re-bound before escaping beyond it. A negligible but nonzero fraction will even do so after crossing the Roche surface since back-scattering can in principle take place between two different escapers or field stars at arbitrarily large r. Even when this does not occur, potential escapers often take significant time (up to gigayears or several relaxation times) to cross beyond the Roche surface (e.g., Fukushige & Heggie 2000), primarily because the escape trajectories may take many crossing times to find and pass through the openings in the Roche surface near the Lagrange points. These openings are very small when the escaper has E_J just above $\phi_{\rm eff}(r_J)$, barely enough to escape. Finally, the trajectories of objects in a rotating frame are complex, made more so by mathematical chaos inherent to the N-body problem. The Coriolis effect in particular can bend trajectories back on themselves, allowing semi-stable retrograde orbits about the cluster center to exist beyond r_J (e.g., Hénon 1970) and past escapers to reenter the cluster at some later time even in the absence of any scattering. Indeed, preliminary results from N. C. Weatherford et al. (2023, in preparation) suggest that the inward flux of previously escaped stars across the spherical surface at $r = r_J$ is significant, about ∼10% of the outward flux by a Hubble time. Note this result rests upon the three-body problem of an escaper orbiting in the combined potential of the cluster and its host galaxy, neglecting interactions with field stars, other nearby star clusters, and molecular clouds. (This is reasonable since diffusive perturbations from such sources are generally quite small since galactic halos inhabit the collisionless regime of stellar dynamics.) Similarly, originally external objects may enter the cluster and become bound due to internal gravitational scattering. Except for full trajectories in direct N-body models and back-scattering more generally, these effects are commonly neglected in GC models, as much larger uncertainties generally exist in regard to the history of the host environment and its (time-dependent) tidal effects; see Section 2.1.3.

A.2. Different Escape Criteria in Cluster Modeling

In addition to the complexities in the theoretical escape criterion, there are modeling nuances to be mindful of, too. Few studies with modern cluster modeling codes use the raw theoretical energy criterion in Equation (A2) to determine when to remove particles from simulations. This has less to do with the underlying physics and more to do with practicality. Equation (A2) is indeed the formally correct criterion for the energy threshold a particle must exceed to *potentially* escape at some future time. In modeling, however, we generally care less about whether a particle is instantaneously bound and more about when we can reasonably remove it from the simulation (happily increasing computational speed) with confidence that doing so will not significantly alter cluster evolution. So modern direct N-body codes typically remove particles from simulations only once the particles are far enough away from the cluster center that they are relatively unlikely to return to within the tidal boundary; several times the tidal radius is a common criterion (e.g., Lee et al. 2006; Moyano Loyola & Hurley 2013; Rodriguez et al. 2016; Kamlah et al. 2022).

Monte Carlo codes also used a radial criterion, removing stars with apocenter $r_a > r_t = r_J$, until a modified version of the energy-based criterion was found to better reproduce the escape rate from direct N-body results (e.g., Giersz et al. 2008; Chatterjee et al. 2010). The reason is apparent in the observation above that r_J is the *maximal* distance to the tidal boundary; stars can satisfy the energy criterion $E_J > \phi_{\rm eff}(r_J)$

Table A3
Escaper Demographics: Cumulative Population Counts and Binarity

	f_b (%) (1)	Total (2)	MS (3)	G (4)	WD (5)	NS (6)	BH (7)	BHBH (8)	BHNS (9)	BHWD (10)	NSNS (11)	NSWD (12)	WDWD (13)	BHMS (14)	NSMS (15)	WDMS (16)
1	4.1	427,266	420,384	348	17,664	4949	1412	125	2	0	2	28	59	29	15	114
2	4.0	201,850	197,457	161	6111	4807	1374	122	1	2	0	18	34	11	10	73
3	3.8	137,932	132,965	118	3928	4732	1398	115	0	2	0	3	24	14	1	42
4	3.9	309,588	303,100	314	11,851	4872	1461	114	0	0	0	3	1	9	1	17
5	3.5	125,024	118,880	147	4111	4812	1457	112	0	1	0	1	0	3	0	8
6	3.3	81,949	75,756	97	2516	4829	1454	122	0	0	0	1	1	9	0	9
7	4.1	352,404	342,152	456	17,629	4999	1421	132	0	0	1	8	2	11	1	30
8	3.4	88,970	81,851	107	3647	4943	1406	120	0	0	0	12	0	2	2	11
9	3.2	64,640	57,525	85	2720	4955	1381	126	0	0	0	4	0	7	1	10
10	4.7								*Disrupted*							
11	3.5	83,823	76,071	131	4276	5026	1238	99	0	0	0	15	3	4	1	37
12	3.0	49,941	42,979	71	2163	5007	1221	102	0	0	0	10	1	5	1	26

Note. The cumulative binary fraction f_b (1) and cumulative number of escapers by type (2–16). Columns 2–7 each list the total number of escaped objects (separately counting the primary and secondary in the case of a binary). Columns 8–16 each list the number of escaped binaries of different types. Throughout all columns, MS = main-sequence star, G = giant (including Hertzsprung gap objects), WD = white dwarf, NS = neutron star, and BH = black hole.

with much lower $r_a > (2/3)r_J$, so the criterion $r_a > r_t = r_J$ dramatically underpredicts the escape rate. The criterion $r_a > 2r_J/3$, meanwhile, would overpredict the escape rate as orbits with $(2/3)r_J < r_a < r_J$ oriented toward/away from the Lagrange points still have $E_J < \phi_{\rm eff}(r_J)$, incapable of escape. However, the energy-based escape criterion requires modification for Monte Carlo codes since they assume a spherical cluster potential. The relevant energy is the orbital energy within only the cluster potential,

$$E = v^2/2 + \phi_c(r) = E_J + \phi_c(r) - \phi_{\rm eff}(r). \quad \text{(A3)}$$

Expanding for clustercentric distances $r \ll R_G$ yields $\phi_{\rm eff}(r) \approx \phi_c(r) + (\Omega^2/2)(z^2 - bx^2)$, where $b = (2, 3)$ for logarithmic and point-mass galactic potentials, respectively—see Equation (5.4) in Spitzer (1987). From Equation (2), $r_J^3 \approx M_C R_G^3/(bM_G)$, so by Kepler's third law the square of the cluster's galactocentric angular velocity is $\Omega^2 \approx GM_G/R_G^3 \approx GM_C/(br_J^3) = -\phi_c(r_J)/(br_J^2)$. From Equations (A2) and (A3), the energy criterion in terms of the orbital energy E within the cluster is then

$$E > \beta\phi_c(r_J); \quad \beta \equiv 3/2 - (bx^2 - z^2)/(2br_J^2) \approx 3/2. \quad \text{(A4)}$$

This criterion can be fully sphericalized by projecting $r/r_J = (x, y, z)/r_J$ randomly onto the unit sphere to obtain $\langle\beta\rangle \equiv 3/2 - (r/r_J)^2/12$. However, since most escapers originate deep within the cluster ($r/r_J \ll 1$), the second term on the right can be neglected as in Equation (A4). The Giersz et al. (2008) energy criterion (Equation (3)) used by CMC modifies this by adding a term making escape slightly harder to account for back-scattering. This back-scattering term decreases with N since individual particles have a less dominant influence on each other in more populous clusters. The MOCCA Monte Carlo code currently implements an even further-updated escape criterion (Giersz et al. 2013) that eliminates the Giersz et al. (2008) criterion's N-dependence, which was only validated against direct N-body models for relatively small N. This update also introduces a lag time to allow particles meeting the energy criterion time to escape the cluster before removing them from the simulation, but has minimal impact on the cluster escape rate (see Giersz et al. 2013) and so has not been incorporated into CMC. This is of little consequence to the analysis in later papers in this series (e.g., N. C. Weatherford et al. 2023, 20004, in preparation), since they directly solve for the time to escape by integrating escaper orbits from the point of ejection to beyond the tidal boundary in the full potential of the cluster and Galaxy.

Finally, note that while the energy-based criterion in CMC best matches direct N-body results for clusters with static tides, the apocenter criterion may work better for cluster models with time-dependent tides from an elliptical orbit within their host galaxy (e.g., Rodriguez et al. 2023). More complex distance-based criteria that better reflect the shape of the tidal boundary may also improve comparison to direct N-body models (e.g., Sollima & Mastrobuono Battisti 2014). These concerns, and tidal physics in the Monte Carlo method more generally, merit further investigation.

ORCID iDs

Newlin C. Weatherford https://orcid.org/0000-0002-9660-9085
Fulya Kıroğlu https://orcid.org/0000-0003-4412-2176
Giacomo Fragione https://orcid.org/0000-0002-7330-027X
Sourav Chatterjee https://orcid.org/0000-0002-3680-2684
Kyle Kremer https://orcid.org/0000-0002-4086-3180
Frederic A. Rasio https://orcid.org/0000-0002-7132-418X

References

Aarseth, S. J., & Heggie, D. C. 1976, A&A, 53, 259
Aarseth, S. J., Tout, C. A., & Mardling, R. A. 2008, The Cambridge N-Body Lectures, 760 (Berlin: Springer)
Amaro-Seoane, P., & Chen, X. 2016, MNRAS, 458, 3075
Ambartsumian, V. A. 1937, AZh, 14, 207
Ambartsumian, V. A. 1938, ZaTsA, 22, 19
Andrews, J. J., & Kalogera, V. 2022, ApJ, 930, 159
Antognini, J. M., Shappee, B. J., Thompson, T. A., & Amaro-Seoane, P. 2014, MNRAS, 439, 1079
Arca Sedda, M., Amaro Seoane, P., & Chen, X. 2021, A&A, 652, A54
Arca Sedda, M., Askar, A., & Giersz, M. 2018, MNRAS, 479, 4652
Arzoumanian, Z., Chernoff, D. F., & Cordes, J. M. 2002, ApJ, 568, 289
Askar, A., Arca Sedda, M., & Giersz, M. 2018, MNRAS, 478, 1844
Astropy Collaboration, Robitaille, T. P., Tollerud, E. J., et al. 2013, A&A, 558, A33
Atallah, D., Trani, A. A., Kremer, K., et al. 2022, arXiv:2211.09670
Bacon, D., Sigurdsson, S., & Davies, M. B. 1996, MNRAS, 281, 830
Banerjee, S., Baumgardt, H., & Kroupa, P. 2010, MNRAS, 402, 371
Baumgardt, H. 2001, MNRAS, 325, 1323
Baumgardt, H. 2017, MNRAS, 464, 2174
Baumgardt, H., Hilker, M., Sollima, A., & Bellini, A. 2019, MNRAS, 482, 5138
Baumgardt, H., & Makino, J. 2003, MNRAS, 340, 227
Baumgardt, H., Makino, J., & Hut, P. 2005, ApJ, 620, 238
Bekenstein, J. D. 1973, ApJ, 183, 657
Belczynski, K., Heger, A., Gladysz, W., et al. 2016, A&A, 594, A97
Bellazzini, M., Ferraro, F. R., & Ibata, R. 2003, AJ, 125, 188
Belokurov, V., Zucker, D. B., Evans, N. W., et al. 2006, ApJL, 642, L137
Binney, J., & Tremaine, S. 2008, Galactic Dynamics (2nd ed.; Princeton, NJ: Princeton Univ. Press)
Blaauw, A. 1961, BAN, 15, 265
Bonaca, A., Naidu, R. P., Conroy, C., et al. 2021, ApJL, 909, L26
Bonnor, W. B., & Rotenberg, M. A. 1961, RSPSA, 265, 109
Breivik, K., Coughlin, S., Zevin, M., et al. 2020, ApJ, 898, 71
Brown, W. R. 2015, ARA&A, 53, 15
Calamida, A., Corsi, C. E., Bono, G., et al. 2008, MmSAI, 79, 347
Casertano, S., & Hut, P. 1985, ApJ, 298, 80
Chandrasekhar, S. 1942, Principles of Stellar Dynamics (Chicago, IL: Univ. Chicago Press)
Chandrasekhar, S. 1943, ApJ, 97, 263
Chandrasekhar, S. 1960, Principles of Stellar Dynamics (New York: Dover)
Chatterjee, S., Fregeau, J. M., Umbreit, S., & Rasio, F. A. 2010, ApJ, 719, 915
Chatterjee, S., Rodriguez, C. L., & Rasio, F. A. 2017, ApJ, 834, 68
Chatterjee, S., Umbreit, S., Fregeau, J. M., & Rasio, F. A. 2013, MNRAS, 429, 2881
Cheng, R. M., & Evans, C. R. 2013, PhRvD, 87, 104010
Chernoff, D. F., & Huang, X. 1996, in IAU Symp. 174, Dynamical Evolution of Star Clusters: Confrontation of Theory and Observations, ed. P. Hut & J. Makino (Dordrecht: Kluwer), 263
Chernoff, D. F., & Weinberg, M. D. 1990, ApJ, 351, 121
Cordes, J. M., Romani, R. W., & Lundgren, S. C. 1993, Natur, 362, 133
Côté, P., Marzke, R. O., West, M. J., & Minniti, D. 2000, ApJ, 533, 869
Da Costa, G. S., & Armandroff, T. E. 1995, AJ, 109, 2533
Davis, D. S., Richer, H. B., King, I. R., et al. 2008, MNRAS, 383, L20
Dinescu, D. I., Girard, T. M., & van Altena, W. F. 1999, AJ, 117, 1792
Duchêne, G., & Kraus, A. 2013, ARA&A, 51, 269
Duquennoy, A., & Mayor, M. 1991, A&A, 248, 485
El-Badry, K., & Rix, H.-W. 2018, MNRAS, 480, 4884
Faber, J., Rasio, F., & Willems, B. 2005, Icar, 175, 248
Fall, S. M., & Zhang, Q. 2001, ApJ, 561, 751
Favata, M., Hughes, S. A., & Holz, D. E. 2004, ApJL, 607, L5
Fellhauer, M., Lin, D. N. C., Bolte, M., Aarseth, S. J., & Williams, K. A. 2003, ApJL, 595, L53
Forbes, D. A., & Bridges, T. 2010, MNRAS, 404, 1203
Forbes, D. A., Strader, J., & Brodie, J. P. 2004, AJ, 127, 3394
Fragione, G., & Gualandris, A. 2019, MNRAS, 489, 4543
Fragione, G., Kocsis, B., Rasio, F. A., & Silk, J. 2022a, ApJ, 927, 231
Fragione, G., & Loeb, A. 2021, MNRAS, 502, 3879

Fragione, G., Loeb, A., Kocsis, B., & Rasio, F. A. 2022b, ApJ, 933, 170
Fragione, G., Martinez, M. A. S., Kremer, K., et al. 2020, ApJ, 900, 16
Fragione, G., Perna, R., & Loeb, A. 2021, MNRAS, 500, 4307
Fregeau, J. M., Cheung, P., Portegies Zwart, S. F., & Rasio, F. A. 2004, MNRAS, 352, 1
Fregeau, J. M., Gürkan, M. A., Joshi, K. J., & Rasio, F. A. 2003, ApJ, 593, 772
Fregeau, J. M., & Rasio, F. A. 2007, ApJ, 658, 1047
Fregeau, J. M., Richer, H. B., Rasio, F. A., & Hurley, J. R. 2009, ApJL, 695, L20
Freitag, M., & Benz, W. 2001, A&A, 375, 711
Freitag, M., Rasio, F. A., & Baumgardt, H. 2006, MNRAS, 368, 121
Fryer, C. L., Belczynski, K., Wiktorowicz, G., et al. 2012, ApJ, 749, 91
Fujii, M. S., & Zwart, S. P. 2011, Sci, 334, 1380
Fukushige, T., & Heggie, D. C. 2000, MNRAS, 318, 753
Gaburov, E., Lombardi, J. C. J., & Portegies Zwart, S. 2010, MNRAS, 402, 105
Gafton, E., Tejeda, E., Guillochon, J., Korobkin, O., & Rosswog, S. 2015, MNRAS, 449, 771
Gaia Collaboration, Brown, A. G. A., Vallenari, A., et al. 2021, A&A, 649, A1
Geller, A. M., Leigh, N. W. C., Giersz, M., Kremer, K., & Rasio, F. A. 2019, ApJ, 872, 165
Gerosa, D., & Kesden, M. 2016, PhRvD, 93, 124066
Gieles, M., Zwart, S. F. P., Baumgardt, H., et al. 2006, MNRAS, 371, 793
Giersz, M., Heggie, D. C., & Hurley, J. R. 2008, MNRAS, 388, 429
Giersz, M., Heggie, D. C., Hurley, J. R., & Hypki, A. 2013, MNRAS, 431, 2184
Gnedin, O. Y., Hernquist, L., & Ostriker, J. P. 1999a, ApJ, 514, 109
Gnedin, O. Y., Lee, H. M., & Ostriker, J. P. 1999b, ApJ, 522, 935
Gnedin, O. Y., & Ostriker, J. P. 1997, ApJ, 474, 223
González, E., Kremer, K., Chatterjee, S., et al. 2021, ApJL, 908, L29
González Prieto, E., Kremer, K., Fragione, G., et al. 2022, ApJ, 940, 131
Goodman, J., & Hernquist, L. 1991, ApJ, 378, 637
Goodman, J., & Hut, P. 1989, Natur, 339, 40
Goodman, J., & Hut, P. 1993, ApJ, 403, 271
Grondin, S. M., Webb, J. J., Leigh, N. W. C., Speagle, J. S., & Khalifeh, R. J. 2023, MNRAS, 518, 4249
Gualandris, A., & Portegies Zwart, S. 2007, MNRAS, 376, L29
Gualandris, A., Portegies Zwart, S., & Eggleton, P. P. 2004, MNRAS, 350, 615
Guillochon, J., Ramirez-Ruiz, E., & Lin, D. 2011, ApJ, 732, 74
Gvaramadze, V. V., Gualandris, A., & Zwart, S. P. 2009, MNRAS, 396, 570
Hansen, B. M. S., & Phinney, E. S. 1997, MNRAS, 291, 569
Harris, C. R., Millman, K. J., van der Walt, S. J., et al. 2020, Natur, 585, 357
Harris, W. E. 1996, AJ, 112, 1487
Heggie, D., & Hut, P. 2003, The Gravitational Million-body Problem: A Multidisciplinary Approach to Star Cluster Dynamics (Cambridge: Cambridge Univ. Press), doi:10.1017/S1743921319006823
Heggie, D. C. 1975, MNRAS, 173, 729
Helmi, A. 2020, ARA&A, 58, 205
Hénon, M. 1960, AnAp, 23, 668
Hénon, M. 1969, A&A, 2, 151
Hénon, M. 1970, A&A, 9, 24
Hénon, M. 1971a, Ap&SS, 13, 284
Hénon, M. H. 1971b, Ap&SS, 14, 151
Heyl, J. 2007, MNRAS, 381, L70
Heyl, J. 2008a, MNRAS, 390, 622
Heyl, J. S. 2008b, MNRAS, 385, 231
Hilker, M., Baumgardt, H., Sollima, A., & Bellini, A. 2020, in IAU Symp. 351, Star Clusters: From the Milky Way to the Early Universe, ed. A. Bragaglia et al. (Cambridge: Cambridge Univ. Press), 451
Hills, J. G. 1975, AJ, 80, 809
Hills, J. G. 1988, Natur, 331, 687
Hobbs, G., Lorimer, D. R., Lyne, A. G., & Kramer, M. 2005, MNRAS, 360, 974
Holley-Bockelmann, K., Gültekin, K., Shoemaker, D., & Yunes, N. 2008, ApJ, 686, 829
Hunter, J. D. 2007, CSE, 9, 90
Hurley, J. R., Aarseth, S. J., & Shara, M. M. 2007, ApJ, 665, 707
Hurley, J. R., Pols, O. R., & Tout, C. A. 2000, MNRAS, 315, 543
Hurley, J. R., Tout, C. A., & Pols, O. R. 2002, MNRAS, 329, 897
Hut, P. 1985, in Dynamics of Star Clusters, Vol. 113 ed. J. Goodman & P. Hut , 231
Hut, P., & Inagaki, S. 1985, ApJ, 298, 502
Hut, P., McMillan, S., & Romani, R. W. 1992, ApJ, 389, 527
Ibata, R., Malhan, K., Martin, N., et al. 2021, ApJ, 914, 123
Ibata, R. A., Gilmore, G., & Irwin, M. J. 1994, Natur, 370, 194
Jeans, J. H. 1919, MNRAS, 79, 408
Jordan, G. C. I., Perets, H. B., Fisher, R. T., & van Rossum, D. R. 2012, ApJL, 761, L23
Joshi, K. J., Nave, C. P., & Rasio, F. A. 2001, ApJ, 550, 691
Joshi, K. J., Rasio, F. A., & Portegies Zwart, S. 2000, ApJ, 540, 969
Kalirai, J. S., Ventura, P., Richer, H. B., et al. 2001, AJ, 122, 3239
Kamlah, A. W. H., Leveque, A., Spurzem, R., et al. 2022, MNRAS, 511, 4060
King, I. 1959, AJ, 64, 351
King, I. R. 1966, AJ, 71, 64
Kıroğlu, F., Lombardi, J. C. J., & Kremer, J. 2022, arXiv:2210.08002
Kremer, K., Chatterjee, S., Ye, C. S., Rodriguez, C. L., & Rasio, F. A. 2019a, ApJ, 871, 38
Kremer, K., Lombardi, J. C., Lu, W., Piro, A. L., & Rasio, F. A. 2022a, ApJ, 933, 203
Kremer, K., Lu, W., Rodriguez, C. L., Lachat, M., & Rasio, F. A. 2019b, ApJ, 881, 75
Kremer, K., Rui, N. Z., Weatherford, N. C., et al. 2021, ApJ, 917, 28
Kremer, K., Ye, C. S., Chatterjee, S., Rodriguez, C. L., & Rasio, F. A. 2018, ApJL, 855, L15
Kremer, K., Ye, C. S., Kıroğlu, F., et al. 2022b, ApJL, 934, L1
Kremer, K., Ye, C. S., Rui, N. Z., et al. 2020, ApJS, 247, 48
Kromer, M., Fink, M., Stanishev, V., et al. 2013, MNRAS, 429, 2287
Kroupa, P. 2001, MNRAS, 322, 231
Kulkarni, S. R., Hut, P., & McMillan, S. J. 1993, Natur, 364, 421
Kundic, T., & Ostriker, J. P. 1995, ApJ, 438, 702
Kyutoku, K., Ioka, K., & Shibata, M. 2013, PhRvD, 88, 041503
Lada, C. J., & Lada, E. A. 2003, ARA&A, 41, 57
Lee, K. H., Lee, H. M., & Sung, H. 2006, MNRAS, 367, 646
Leonard, P. J. T. 1991, AJ, 101, 562
Leonard, P. J. T., & Duncan, M. J. 1988, AJ, 96, 222
Leonard, P. J. T., & Duncan, M. J. 1990, AJ, 99, 608
Lin, D., Strader, J., Carrasco, E. R., et al. 2018, NatAs, 2, 656
Liu, S.-F., Guillochon, J., Lin, D. N. C., & Ramirez-Ruiz, E. 2013, ApJ, 762, 37
Lousto, C. O., Campanelli, M., Zlochower, Y., & Nakano, H. 2010, CQGra, 27, 114006
Lousto, C. O., & Zlochower, Y. 2008, PhRvD, 77, 044028
Lousto, C. O., & Zlochower, Y. 2009, PhRvD, 79, 064018
Lousto, C. O., & Zlochower, Y. 2011, PhRvL, 107, 231102
Lousto, C. O., Zlochower, Y., Dotti, M., & Volonteri, M. 2012, PhRvD, 85, 084015
Lynden-Bell, D., Wood, R., & Royal, A. 1968, MNRAS, 138, 495
Lyne, A. G., Anderson, B., & Salter, M. J. 1982, MNRAS, 201, 503
Lyne, A. G., & Lorimer, D. R. 1994, Natur, 369, 127
Mackey, A. D., Wilkinson, M. I., Davies, M. B., & Gilmore, G. F. 2007, MNRAS, 379, L40
Mackey, A. D., Wilkinson, M. I., Davies, M. B., & Gilmore, G. F. 2008, MNRAS, 386, 65
Madrid, J. P., Hurley, J. R., & Martig, M. 2014, ApJ, 784, 95
Maliszewski, K., Giersz, M., Gondek-Rosinska, D., Askar, A., & Hypki, A. 2022, MNRAS, 514, 5879
Mandushev, G., Staneva, A., & Spasova, N. 1991, A&A, 252, 94
Manukian, H., Guillochon, J., Ramirez-Ruiz, E., & O'Leary, R. M. 2013, ApJL, 771, L28
Mardling, R. A., & Aarseth, S. J. 2001, MNRAS, 321, 398
Martin, N. F., Ibata, R. A., Bellazzini, M., et al. 2004, MNRAS, 348, 12
Mateu, C. 2023, MNRAS, in press
McLaughlin, D. E., & Fall, S. M. 2008, ApJ, 679, 1272
McMillan, S. L. W. 1986, ApJ, 306, 552
Merritt, D., Milosavljević, M., Favata, M., Hughes, S. A., & Holz, D. E. 2004a, ApJL, 607, L9
Merritt, D., Piatek, S., Portegies Zwart, S., & Hemsendorf, M. 2004b, ApJL, 608, L25
Milone, A. P., Piotto, G., Bedin, L. R., et al. 2012, A&A, 540, A16
Moe, M., & Di Stefano, R. 2017, ApJS, 230, 15
Moody, K., & Sigurdsson, S. 2009, ApJ, 690, 1370
Morawski, J., Giersz, M., Askar, A., & Belczynski, K. 2018, MNRAS, 481, 2168
Morscher, M., Pattabiraman, B., Rodriguez, C., Rasio, F. A., & Umbreit, S. 2015, ApJ, 800, 9
Morscher, M., Umbreit, S., Farr, W. M., & Rasio, F. A. 2013, ApJL, 763, L15
Moyano Loyola, G. R. I., & Hurley, J. R. 2013, MNRAS, 434, 2509
Myeong, G. C., Evans, N. W., Belokurov, V., Sanders, J. L., & Koposov, S. E. 2018, ApJL, 863, L28
Odenkirchen, M., Grebel, E. K., Rockosi, C. M., et al. 2001, ApJL, 548, L165

O'Leary, R. M., Rasio, F. A., Fregeau, J. M., Ivanova, N., & O'Shaughnessy, R. 2006, ApJ, 637, 937
Ostriker, J. P., Spitzer, L., Jr., & Chevalier, R. A. 1972, ApJL, 176, L51
Pattabiraman, B., Umbreit, S., Liao, W.-k., et al. 2013, ApJS, 204, 15
Peebles, P. J. E., & Dicke, R. H. 1968, ApJ, 154, 891
Peres, A. 1962, PhRv, 128, 2471
Perets, H. B., & Šubr, L. 2012, ApJ, 751, 133
Peuten, M., Zocchi, A., Gieles, M., Gualandris, A., & Henault-Brunet, V. 2016, MNRAS, 462, 2333
Pfahl, E. 2005, ApJ, 626, 849
Piatti, A. E., & Carballo-Bello, J. A. 2020, A&A, 637, L2
Prieto, J. L., & Gnedin, O. Y. 2008, ApJ, 689, 919
Rasskazov, A., Fragione, G., & Kocsis, B. 2020, ApJ, 899, 149
Reback, J., jbrockmendel, McKinney, W., et al. 2022, pandas-dev/pandas: Pandas v1.4.2, Zenodo, doi:10.5281/zenodo.3509134
Rees, M. J. 1988, Natur, 333, 523
Repetto, S., Igoshev, A. P., & Nelemans, G. 2017, MNRAS, 467, 298
Rodgers, A. W., & Paltoglou, G. 1984, ApJL, 283, L5
Rodriguez, C. L., Amaro-Seoane, P., Chatterjee, S., & Rasio, F. A. 2018a, PhRvL, 120, 151101
Rodriguez, C. L., Amaro-Seoane, P., Chatterjee, S., et al. 2018b, PhRvD, 98, 123005
Rodriguez, C. L., Coughlin, S. C., Weatherford, N. C., et al. 2021, ClusterMonteCarlo/CMC-COSMIC: Release Version of CMC, v1.0.0, Zenodo, doi:10.5281/zenodo.4850884
Rodriguez, C. L., Hafen, Z., Grudić, M. Y., et al. 2023, MNRAS, 521, 124
Rodriguez, C. L., Morscher, M., Wang, L., et al. 2016, MNRAS, 463, 2109
Rodriguez, C. L., Pattabiraman, B., Chatterjee, S., et al. 2018c, ComAC, 5, 5
Rodriguez, C. L., Weatherford, N. C., Coughlin, S. C., et al. 2022, ApJS, 258, 22
Rosswog, S., Davies, M. B., Thielemann, F. K., & Piran, T. 2000, A&A, 360, 171
Rui, N. Z., Kremer, K., Weatherford, N. C., et al. 2021a, ApJ, 912, 102
Rui, N. Z., Weatherford, N. C., Kremer, K., et al. 2021b, RNAAS, 5, 47
Ryu, T., Krolik, J., Piran, T., & Noble, S. C. 2020a, ApJ, 904, 98
Ryu, T., Krolik, J., Piran, T., & Noble, S. C. 2020b, ApJ, 904, 99
Ryu, T., Krolik, J., Piran, T., & Noble, S. C. 2020c, ApJ, 904, 100
Ryu, T., Perna, R., Pakmor, R., et al. 2023, MNRAS, 519, 5787
Samsing, J., Venumadhav, T., Dai, L., et al. 2019, PhRvD, 100, 043009
Searle, L., & Zinn, R. 1978, ApJ, 225, 357
Sigurdsson, S., & Phinney, E. S. 1993, ApJ, 415, 631
Sollima, A., & Mastrobuono Battisti, A. 2014, MNRAS, 443, 3513
Spitzer, L. 1987, Dynamical Evolution of Globular Clusters (Princeton, NJ: Princeton Univ. Press)
Spitzer, L., Jr. 1940, MNRAS, 100, 396
Spitzer, L., Jr., & Chevalier, R. A. 1973, ApJ, 183, 565
Spitzer, L., Jr., & Shapiro, S. L. 1972, ApJ, 173, 529
Spitzer, L., Jr., & Shull, J. M. 1975, ApJ, 201, 773
Statler, T. S., Ostriker, J. P., & Cohn, H. N. 1987, ApJ, 316, 626
Šubr, L., Fragione, G., & Dabringhausen, J. 2019, MNRAS, 484, 2974
Toonen, S., Boekholt, T. C. N., & Portegies Zwart, S. 2022, A&A, 661, A61
van den Bergh, S. 1993, ApJ, 411, 178
Vasiliev, E., & Baumgardt, H. 2021, MNRAS, 505, 5978
Virtanen, P., Gommers, R., Oliphant, T. E., et al. 2020, NatMe, 17, 261
Vitral, E., Kremer, K., Libralato, M., Mamon, G. A., & Bellini, A. 2022, MNRAS, 514, 806
Weatherford, N. C., Chatterjee, S., Kremer, K., & Rasio, F. A. 2020, ApJ, 898, 162
Weatherford, N. C., Chatterjee, S., Rodriguez, C. L., & Rasio, F. A. 2018, ApJ, 864, 13
Weatherford, N. C., Fragione, G., Kremer, K., et al. 2021, ApJL, 907, L25
Webb, J. J., Harris, W. E., Sills, A., & Hurley, J. R. 2013, ApJ, 764, 124
Webb, J. J., Sills, A., Harris, W. E., & Hurley, J. R. 2014, MNRAS, 445, 1048
Weidemann, V. 1977, A&A, 61, L27
Ye, C. S., Kremer, K., Chatterjee, S., Rodriguez, C. L., & Rasio, F. A. 2019, ApJ, 877, 122
Ye, C. S., Kremer, K., Rodriguez, C. L., et al. 2022, ApJ, 931, 84
Yuan, Z., Chang, J., Beers, T. C., & Huang, Y. 2020, ApJL, 898, L37
Zinn, R. 1985, ApJ, 293, 424
Zinn, R. 1993, in ASP Conf. Ser. 48, The Globular Cluster-galaxy Connection, ed. G. H. Smith & J. P. Brodie (San Francisco, CA: ASP), 38
Zocchi, A., Gieles, M., & Hénault-Brunet, V. 2019, MNRAS, 482, 4713